

# *Lone pair rotation and bond heterogeneity leading to ultralow thermal conductivity in aikinite*

Article

Published Version

Creative Commons: Attribution 4.0 (CC-BY)

Open Access

Carnevali, V., Mukherjee, S., Voneshen, D. J., Maji, K., Guilmeau, E., Powell, A. V., Vaqueiro, P. ORCID: <https://orcid.org/0000-0001-7545-6262> and Fornari, M. (2023) Lone pair rotation and bond heterogeneity leading to ultralow thermal conductivity in aikinite. *Journal of the American Chemical Society*, 145 (16). pp. 9313-9325. ISSN 0002-7863 doi: <https://doi.org/10.1021/jacs.3c02536> Available at <https://centaur.reading.ac.uk/111416/>

It is advisable to refer to the publisher's version if you intend to cite from the work. See [Guidance on citing](#).

To link to this article DOI: <http://dx.doi.org/10.1021/jacs.3c02536>

Publisher: American Chemical Society

All outputs in CentAUR are protected by Intellectual Property Rights law, including copyright law. Copyright and IPR is retained by the creators or other copyright holders. Terms and conditions for use of this material are defined in the [End User Agreement](#).

[www.reading.ac.uk/centaur](http://www.reading.ac.uk/centaur)

**CentAUR**

Central Archive at the University of Reading

Reading's research outputs online

# Lone Pair Rotation and Bond Heterogeneity Leading to Ultralow Thermal Conductivity in Aikinite

Virginia Carnevali,<sup>¶</sup> Shriparna Mukherjee,<sup>¶</sup> David J. Voneshen, Krishnendu Maji, Emmanuel Guilmeau, Anthony V. Powell, Paz Vaqueiro,<sup>\*</sup> and Marco Fornari<sup>\*</sup>



Cite This: *J. Am. Chem. Soc.* 2023, 145, 9313–9325



Read Online

ACCESS |



Metrics & More

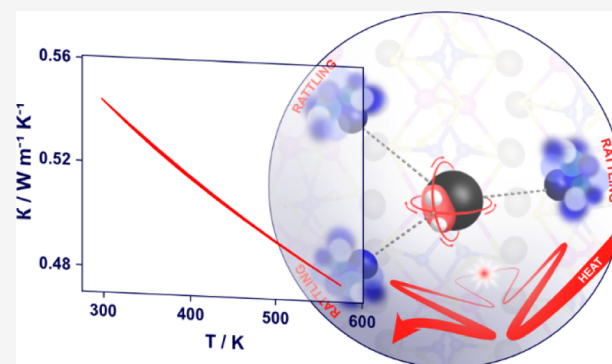


Article Recommendations



Supporting Information

**ABSTRACT:** Understanding the relationship between the crystal structure, chemical bonding, and lattice dynamics is crucial for the design of materials with low thermal conductivities, which are essential in fields as diverse as thermoelectrics, thermal barrier coatings, and optoelectronics. The bismuthinite-aikinite series,  $\text{Cu}_{1-x}\square_x\text{Pb}_{1-x}\text{Bi}_{1+x}\text{S}_3$  ( $0 \leq x \leq 1$ , where  $\square$  represents a vacancy), has recently emerged as a family of *n*-type semiconductors with exceptionally low lattice thermal conductivities. We present a detailed investigation of the structure, electronic properties, and the vibrational spectrum of aikinite,  $\text{CuPbBiS}_3$  ( $x = 0$ ), in order to elucidate the origin of its ultralow thermal conductivity ( $0.48 \text{ W m}^{-1} \text{ K}^{-1}$  at 573 K), which is close to the calculated minimum for amorphous and disordered materials, despite its polycrystalline nature. Inelastic neutron scattering data reveal an anharmonic optical phonon mode at *ca.*  $30 \text{ cm}^{-1}$ , attributed mainly to the motion of  $\text{Pb}^{2+}$  cations. Analysis of neutron diffraction data, together with *ab-initio* molecular dynamics simulations, shows that the  $\text{Pb}^{2+}$  lone pairs are rotating and that, with increasing temperature,  $\text{Cu}^+$  and  $\text{Pb}^{2+}$  cations, which are separated at distances of *ca.*  $3.3 \text{ \AA}$ , exhibit significantly larger displacements from their equilibrium positions than  $\text{Bi}^{3+}$  cations. In addition to bond heterogeneity, a temperature-dependent interaction between  $\text{Cu}^+$  and the rotating  $\text{Pb}^{2+}$  lone pair is a key contributor to the scattering effects that lower the thermal conductivity in aikinite. This work demonstrates that coupling of rotating lone pairs and the vibrational motion is an effective mechanism to achieve ultralow thermal conductivity in crystalline materials.



## INTRODUCTION

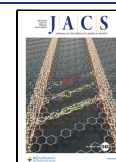
Thermal transport is of paramount importance for a broad range of technological applications. For instance, thermally insulating materials can be used to prevent heat from damaging critical components,<sup>1</sup> and the performance, safety, and lifetime of batteries in electric vehicles can be improved with optimized thermal management.<sup>2</sup> Finding materials that combine the desired thermal conductivity with other properties required for specific technological applications can be exceptionally challenging. This is the case for thermoelectric devices, which enable the conversion of a temperature difference into electrical power. For thermoelectric applications, materials with low thermal conductivity are required in order to limit parasitic heat transfer. However, these materials also need to be excellent electrical conductors; this is a conflicting requirement because heat is transported by electrons as well as by phonons. A variety of extrinsic and intrinsic strategies have been proposed in order to minimize phonon transport (which determines the lattice thermal conductivity,  $\kappa_L$ ) in thermoelectric materials.<sup>3</sup> While extrinsic effects, such as multiscale hierarchical structuring,<sup>4</sup> grain-boundary engineering,<sup>5</sup> and nanoprecipitates,<sup>6</sup> are effective at lowering  $\kappa_L$ , they can also adversely influence other

properties, such as mechanical and thermal stability, as well as the charge-carrier mobility. Recent research efforts have focused on intrinsic mechanisms that reduce  $\kappa_L$  by tuning the structure and bonding of materials. These mechanisms include complex crystal structures with a large number of atoms per unit cell,<sup>7</sup> order–disorder phenomena,<sup>8,9</sup> liquid-like ionic mobility (phonon–liquid–electron–crystal),<sup>10</sup> rattling,<sup>11</sup> resonant bonding,<sup>12</sup> anharmonicity induced by lone pairs,<sup>13</sup> and bonding heterogeneity.<sup>14,15</sup>

The efficiency of thermoelectric energy recovery is related to the figure of merit,  $ZT = \sigma S^2 T / (\kappa_e + \kappa_L)$  (where  $\sigma$ ,  $S$ ,  $T$ ,  $\kappa_e$ , and  $\kappa_L$  are the electrical conductivity, the Seebeck coefficient, the operating temperature, and the electronic and lattice components of the thermal conductivity, respectively) of the thermoelectric materials found in the device.<sup>16</sup> Among the

Received: March 9, 2023

Published: April 13, 2023



chalcogenides, sulfide-based minerals are attractive as potential thermoelectric materials due to the large terrestrial abundance and availability of sulfur when compared to selenium and tellurium.<sup>17</sup> A feature common to many of the best performing thermoelectric sulfides is their low thermal conductivity, the origin of which is not fully understood. Promising *p*-type sulfide minerals, with a thermoelectric figure of merit,  $ZT$ , approaching unity at moderate temperatures and low thermal conductivity, include tetrahedrites,  $\text{Cu}_{12+x}\text{Sb}_4\text{S}_{13}$ <sup>18,19</sup> and  $\text{Cu}_{12-x}\text{M}_x\text{Sb}_4\text{S}_{13}$  ( $M = \text{Zn}, \text{Ni}$ ),<sup>20–22</sup> colusites,  $\text{Cu}_{26}\text{T}_2\text{M}_6\text{S}_{32}$  ( $T = \text{Cr}, \text{Mo}$  and  $\text{W}$ , and  $M = \text{Ge}$  and  $\text{Sn}$ )<sup>23–26</sup> and bornite,  $\text{Cu}_5\text{FeS}_4$ .<sup>27</sup> By contrast, progress on the corresponding *n*-type sulfides has been limited,<sup>28</sup> with several bismuth-containing sulfides being among the best *n*-type candidates for thermoelectric applications at moderate temperatures. For instance, bismuthinite,  $\text{Bi}_2\text{S}_3$ , reaches  $ZT \approx 0.6$  at 773 K when doped with chlorine,<sup>29</sup> while  $\text{CdPb}_2\text{Bi}_4\text{S}_9$ , which is a member of the pavonite-homologous series,  $\text{M}_{n+1}\text{Bi}_2\text{Q}_{n+5}$  ( $n = 4$ ), exhibits a figure of merit,  $ZT = 0.53$  at 775 K.<sup>30</sup>

Very recently, it has been reported that the quaternary sulfide  $\text{CuPbBi}_5\text{S}_9$  exhibits ultralow thermal conductivity,  $\kappa \approx 0.5 \text{ W m}^{-1} \text{ K}^{-1}$ , and can reach  $ZT = 0.43$  at 700 K upon doping.<sup>31,32</sup> This material is a member ( $x = 2/3$ ) of the bismuthinite-aikinite series,  $\text{Cu}_{1-x}\text{Pb}_x\text{Bi}_{1+x}\text{S}_3$  ( $0 \leq x \leq 1$ ), all of which exhibit closely related crystal structures (Figure 1).<sup>33,34</sup> The structure of

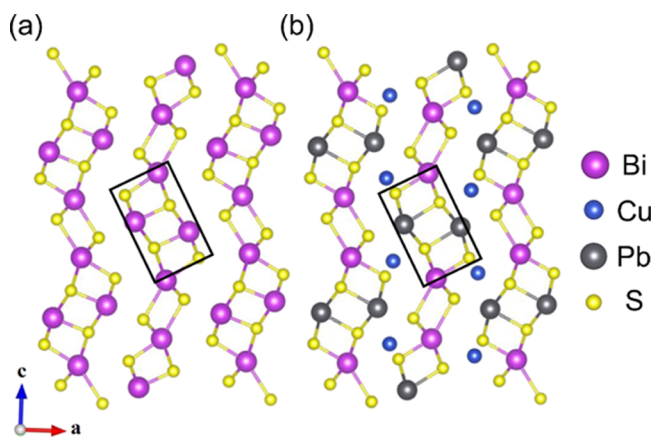


**Figure 1.** Comparison of the structures of (a)  $\text{Bi}_2\text{S}_3$  and (b)  $\text{CuPbBiS}_3$  (space group,  $Pnma$ ); the black rectangle highlights the  $\text{Bi}_4\text{S}_6$  ribbons in  $\text{Bi}_2\text{S}_3$  and the  $\text{Bi}_2\text{Pb}_2\text{S}_6$  ribbons in aikinite.

bismuthinite,  $\text{Bi}_2\text{S}_3$  ( $x = 1$ ), which is highly anisotropic, contains  $\text{Bi}_4\text{S}_6$  ribbons arranged in a herringbone pattern. In aikinite ( $x = 0$ ), half of the  $\text{Bi}^{3+}$  cations are replaced with  $\text{Pb}^{2+}$ , with  $\text{Cu}^+$  cations filling the tetrahedral holes between the  $\text{Bi}_2\text{Pb}_2\text{S}_6$  ribbons. In the bismuthinite-aikinite series, the aikinite end member ( $x = 0$ ), as well as krupaitite,  $\text{CuPbBi}_3\text{S}_6$  ( $x = 0.5$ ), adopt unit cells based on the archetype illustrated in Figure 1b. In natural specimens, minerals with intermediate compositions exhibit superstructures based on the ordered intergrowth of blocks of bismuthinite, aikinite, and krupaitite.<sup>35</sup> However, cation ordering is extremely slow, and synthetic materials with intermediate compositions adopt a copper-deficient aikinite structure, which contains disordered vacancies at the tetrahedral copper site.<sup>36</sup>

Despite the large number of minerals in the aikinite-bismuthinite series, little is known about the electrical and thermal transport properties of these materials, with the exception of those of  $\text{Bi}_2\text{S}_3$  and  $\text{CuPbBi}_5\text{S}_9$ ,<sup>29,31</sup> which are *n*-

type semiconductors. Here, we present a detailed study of the structure and transport properties of aikinite,  $\text{CuPbBiS}_3$ , from experimental and theoretical points of view. We demonstrate that  $\text{CuPbBiS}_3$  is a crystalline *p*-type semiconductor with ultralow lattice thermal conductivity, close to the minimum lattice thermal conductivity calculated on the basis of Cahill's model<sup>37</sup> for amorphous and disordered materials. Although neutron diffraction data indicate that in the crystal structure of aikinite the  $\text{Cu}^+$ ,  $\text{Pb}^{2+}$ , and  $\text{Bi}^{3+}$  cations are fully ordered, our sound velocity measurements reveal that, at room temperature, the phonon mean-free-path is only *ca.* 5 Å, which is approximately twice that of the interatomic spacing. The temperature dependence of the vibrational spectrum has been investigated by *ab-initio* molecular dynamics (AIMD), while inelastic neutron scattering (INS) data have been exploited to estimate the lifetime of the low-frequency  $\text{Pb}^{2+}$  mode, which is only *ca.* 0.4 ps. Our analysis of the calculated and experimental vibrational density of states ( $\nu\text{DOS}$ ), which are in excellent agreement, provides clear evidence for the presence of  $\text{Cu}^+$  rattling-like modes, together with anharmonic low-energy modes arising from weakly bonded  $\text{Pb}^{2+}$  cations. *Ab-initio* molecular dynamics simulations reveal that the intrinsic mechanism responsible for the ultralow thermal conductivity in aikinite entails the cooperative interaction between the rotating lone pair on the  $\text{Pb}^{2+}$  cations and the  $\text{Cu}^+$  cations.

## EXPERIMENTAL AND COMPUTATIONAL SECTION

**Material Synthesis.**  $\text{CuPbBiS}_3$  was prepared by mechanical alloying of stoichiometric amounts of Cu (Sigma-Aldrich, powder 425  $\mu\text{m}$ , 99.5%), Pb (Goodfellow, rods 3.2 mm dia., 99.95%), Bi (Alfa Aesar, needles, 99.99%), and S (Sigma-Aldrich, flakes, 99.99%). The reagents were handled under an Ar atmosphere, inside a glovebox. Prior to loading the elements into a 45 mL ball-milling jar made of stainless steel, the Pb rods were cut into small pieces, and Bi needles were ground into a powder using a pestle and mortar. Eighteen stainless-steel balls, each with a diameter of 10 mm and a weight of 4 g, were added to the ball-milling jar. A powder-to-ball weight ratio of 1:12 was used. Milling was carried out using a Fritsch Pulverisette 6 Planetary Ball Mill at 500 rpm for 60 h and stopped for 10 min every 10 min of milling. Following milling, the resulting powder was sealed into an evacuated ( $<10^{-4}$  mbar) fused-silica ampoule. The sealed ampoule was heated to 573 K (at a rate of 1 K  $\text{min}^{-1}$ ), held for 48 h at this temperature, and subsequently cooled to room temperature (at a rate of 1 K  $\text{min}^{-1}$ ). The annealed powder was hand-ground in air and consolidated into a densified pellet of *ca.* 13 mm diameter by hot pressing under  $\text{N}_2$  at 473 K under 80 MPa for 1 h. The pressure was released, and the hot press was then cooled down for 1 h to room temperature. The density of the hot-pressed pellet was determined by the Archimedes' method, using an AE Adam PW 184 balance. The pellet has a density greater than 96% of the crystallographic density of aikinite.

### X-ray and Neutron Diffraction Data Collection and Analysis.

Powder X-ray diffraction data were collected on a Bruker D8 Advance powder X-ray diffractometer equipped with a LynxEye detector and operating with monochromatic  $\text{Cu K}\alpha 1$  ( $\lambda = 1.54046 \text{ \AA}$ ) radiation. Data collections of 8 h over the range  $10 \leq 2\theta^\circ \leq 120$  were used. Lattice parameters were determined by the Rietveld method, carried out using GSAS.<sup>38</sup> A shifted Chebyshev polynomial with ten coefficients was used to model the background, and a pseudo-Voigt function was used to model the peak shape. High-resolution neutron powder diffraction data were collected on the time-of-flight POWGEN beamline<sup>39</sup> at the Spallation Neutron Source (Oak Ridge National Laboratory, US). Data were collected at room temperature for 3 h using the center wavelength setting of 1.5 Å, with a *d*-spacing coverage of  $0.5 \leq d/\text{\AA} \leq 11.8$ . The powder sample was loaded into a vanadium can with an 8 mm inner diameter and sealed with a copper gasket and aluminum lid. Rietveld refinements using neutron data were carried out using GSAS-II.<sup>40</sup> A logarithmic interpolation function with twenty terms was

used to model the background contribution. Lattice parameters, atomic coordinates, profile parameters, and the phase fraction for both aikinite and PbS were refined. A single isotropic atomic displacement parameter ( $U_{\text{iso}}$ ) was used for all the sulfur atoms in the aikinite phase and refined along with those of copper, lead, and bismuth atoms. Different structural models for the aikinite phase were explored, as detailed in the results section.

**Optical Measurements.** A diffuse reflectance measurement was carried out over the wavelength range  $200 \leq \lambda/\text{nm} \leq 2500$  with a step size of 1 nm using an Agilent Cary 7000 spectrophotometer equipped with a diffuse reflectance accessory. The reflectance data were transformed into the corresponding absorption spectra using the Kubelka–Munk function,  $F(R_{\infty}) = \frac{K}{S} = \frac{(1 - R_{\infty})^2}{2R_{\infty}}$ , where  $R_{\infty}$  is the reflectance of an infinitely thick specimen and  $K$  and  $S$  are the absorption and scattering coefficients, respectively. The band gap ( $E_g$ ) was estimated using the Tauc method,<sup>41</sup> from the linear fit of  $(F(R_{\infty})h\nu)^{1/n} = A(h\nu - E_g)$  vs.  $h\nu$ , where  $A$  is a proportionality constant,  $h$  is Planck's constant,  $\nu$  is the photon frequency, and  $n = 1/2$  or  $2$  for direct and indirect transitions, respectively.

**Thermal and Electrical Property Measurements.** Differential scanning calorimetry (DSC) data over the temperature range  $300 \leq T/K \leq 575$  and a heating rate of  $10 \text{ K min}^{-1}$  were collected under a flowing  $\text{N}_2$  atmosphere using a TA-Q2000 DSC instrument. Thermogravimetric analysis (TGA) was carried out over the temperature range  $300 \leq T/K \leq 970$  using a TA-TGA Q50 under a  $\text{N}_2$  atmosphere; a heating rate of  $10 \text{ K min}^{-1}$  was used. The electrical conductivity and Seebeck coefficient were measured simultaneously using a Linseis LSR 3 instrument, using a 4-probe configuration, under a helium atmosphere. Measurements were carried out on pellets with a diameter of 12.7 mm and thickness of  $\sim 1.5$ – $2$  mm. The electrical conductivity and Seebeck coefficient were measured over the temperature range of  $423 \leq T/K \leq 573$ . A current of 20 mA was used for the conductivity measurements, and a maximum gradient of 50 K was maintained between the upper and lower electrodes for the measurement of the Seebeck coefficient. The instrument was calibrated using a constantan reference. Thermal diffusivity ( $D$ ) measurements were made on graphite-coated circular pellets with a diameter of 12.7 mm and a thickness of  $\sim 1.5$ – $2$  mm, using a Netzsch LFA 447 NanoFlash system, over the temperature range of  $273 \leq T/K \leq 573$ . Data were analyzed using Cowan's model with a pulse correction applied. The thermal conductivity ( $\kappa$ ) was then calculated from the relation,  $\kappa = DdC_p$ , where  $d$  is the density of the material and  $C_p$  is the specific heat capacity. The Dulong–Petit limit for  $C_p$ , which for  $\text{CuPbBiS}_3$  is  $0.259 \text{ J g}^{-1} \text{ K}^{-1}$ , has been used. The uncertainties in the values of the electrical resistivity, Seebeck coefficient, and thermal conductivity are 5, 5, and 10% respectively. The calculations of the minimum thermal conductivity are described in the Supporting Information. The Lorenz number  $L$  was determined using the relation  $L = 1.5 + \exp(-|S|/116)$ ,<sup>42</sup> where  $S$  is the temperature-dependent Seebeck coefficient. Using the Wiedemann–Franz relation, the electronic part of thermal conductivity  $\kappa_e$  was calculated. Hall effect measurements, to determine the charge carrier concentration, were carried out at room temperature using a physical properties measurement system (PPMS, Quantum Design) under applied magnetic fields of up to 9 T.

**Sound Velocity Measurements.** The transverse ( $v_T$ ) and longitudinal velocities ( $v_L$ ) of sound were measured on a disc-shaped sample of ca. 12.5 mm diameter and ca. 2 mm thickness using an Olympus ultrasonic flaw detector (model 38DL plus) with a transducer frequency of 5 MHz.

**Inelastic Neutron Scattering Data.** INS data were collected using the LET spectrometer (ISIS Neutron and Muon Source, UK).<sup>43</sup> The powder sample was loaded into an annular aluminum can. Data were collected at four temperatures, i.e., 10, 100, 200, and 300 K. The LET choppers were set up to use incident energies of 24.93, 9.01, 4.60, and 2.79 meV. Identical measurements were carried out for the empty aluminum can, and the instrumental background was subtracted using the Mantid package.<sup>44,45</sup> The INS data were integrated from 3 to  $5 \text{ \AA}^{-1}$  in  $Q$ -space. The neutron-weighted phonon density of states was normalized using a custom Python script. The phonon energies were

analyzed using the DAVE package.<sup>46</sup> Peaks were modeled using individual Gaussian functions.

**Electronic Bands and Transport.** *Ab-initio* electronic calculations were performed using Quantum ESPRESSO<sup>47</sup> as incorporated in the high-throughput infrastructure AFLOW $\pi$ .<sup>48</sup> We used ultrasoft PBE pseudopotentials, well-converged basis sets corresponding to an energy cutoff of 60 Ry for the wave functions and 600 Ry for the charge density, and the ACBN0 approach<sup>49</sup> to self-consistently determine the values for the Hubbard corrections for each atomic species of the material ( $U(\text{Pb}) = 0.003 \text{ eV}$ ,  $U(\text{Cu}) = 3.403 \text{ eV}$ ,  $U(\text{Bi}) = 0.014 \text{ eV}$ , and  $U(\text{S}) = 1.589 \text{ eV}$ ). Hubbard corrections were applied to the 3d orbitals of Cu, the 6p orbitals of Pb and Bi, and the 3p orbitals of S. Spin–orbit coupling was included in the calculation. To integrate over the Brillouin zone, we used a  $4 \times 8 \times 4$  Monkhorst–Pack k-point mesh.<sup>50</sup> The optimized theoretical lattice parameters used for the *ab-initio* simulations are  $a = 11.943 \text{ \AA}$ ,  $b = 4.058 \text{ \AA}$ , and  $c = 11.321 \text{ \AA}$ . The effective masses have been computed with the method developed by Supka *et al.*<sup>51</sup>

**Born–Oppenheimer Ab-Initio Molecular Dynamics.** AIMD simulations with the mixed Gaussian and plane wave (GPW) method as implemented in the CP2K package<sup>52</sup> were performed to compute the vibrational and structural properties of aikinite as a function of temperature. Valence electrons were expanded as a double- $\zeta$  Gaussian basis set with polarization functions (DZVP).<sup>53</sup> The energy cutoff for the electron density expansion in the GPW method was 400 Ry. The temperature was controlled by the velocity-rescaling thermostat of Bussi *et al.*<sup>54</sup> with a time constant of 1.0 fs. The system was first equilibrated to 300 K for 10 ps in the isothermal-isobaric ensemble (NPT) with  $P = 1 \text{ atm}$ . The system was then equilibrated in the microcanonical (NVE) ensemble, and statistics were gathered for the last 10 ps of the production run. Maximally localized Wannier functions (MLWF)<sup>55</sup> and their centers (MLWFC) were obtained using CP2K, minimizing the MLWF spreads as explained by Berghold *et al.*<sup>56</sup> The  $\text{Pb}^{2+}$  lone pair dynamics has been characterized through the rotational time correlation function (TCF)<sup>57</sup>

$$C_{\text{rot}}(t) = \langle P_2(\text{dip}(t) \cdot \text{dip}(0)) \rangle$$

where  $\text{dip}(t)$  is the  $\text{Pb}^{2+}$  MLWFC dipole moment at time  $t$ , and  $P_2(x)$  is the second-order Legendre polynomial.

**Vibrational Properties.** Phonon dispersions and the vDOS for aikinite were reported by Maji *et al.*<sup>26</sup> and serve as a starting point for the computation of the lattice thermal conductivity in the quasi-harmonic approximations.<sup>58,59</sup> The transverse and longitudinal sound velocities have been derived in two different ways: from the phonon dispersion and from the computed elastic constants (see Supporting Information). All AIMD simulations were performed at the  $\Gamma$ -point in a  $2 \times 5 \times 2$  supercell. The lattice parameters of the triclinic simulation box were allowed to relax for 10 ps in the NPT ensemble with  $P = 1 \text{ atm}$ . The system was then equilibrated over 5 ps in the isothermal-isochoric ensemble (NVT) using the supercell volume obtained by the NPT runs; 20 ps of simulation were used to estimate temperature-dependent effects at 100, 200, and 300 K. The vDOS,  $D(\omega)$ , was calculated as a Fourier transform of the velocity autocorrelation function (VACF) as

$$D(\omega) = \frac{1}{3Nk_B T} \int_0^\infty \frac{\langle \mathbf{v}(0) \cdot \mathbf{v}(t) \rangle}{\langle \mathbf{v}(0) \cdot \mathbf{v}(0) \rangle} e^{i\omega t} dt$$

where  $\langle \mathbf{v}(0) \cdot \mathbf{v}(t) \rangle$  is the VACF computed over the production's run trajectory,  $\omega$  is the frequency,  $N$  is the number of atoms,  $k_B$  is the Boltzmann constant, and  $T$  is the absolute temperature. We found good agreement between the Quantum ESPRESSO and the CP2K results when comparisons were possible. From the calculated vDOS, we have also computed the Helmholtz free energy  $F$ , the internal energy  $E$ , the entropy  $S$ , and the specific heat  $C_v$  at zero pressure (Supporting Information, Figure S1).

## RESULTS AND DISCUSSION

**Crystal Structure and Bonding.** Powder X-ray diffraction data collected at room temperature can be indexed on an

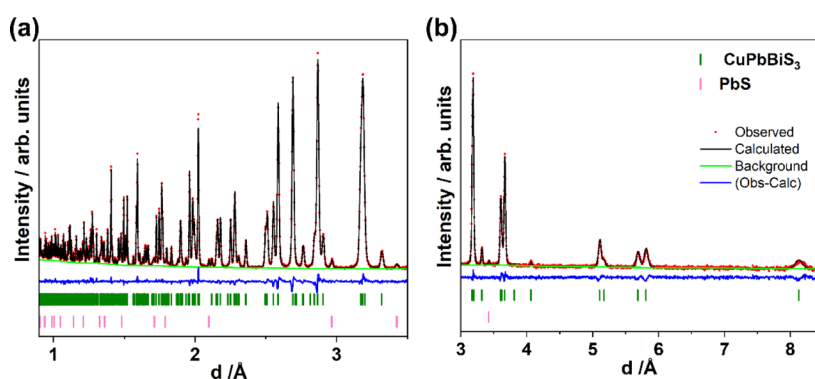


**Figure 2.** Rietveld refinement using neutron diffraction data for  $\text{CuPbBiS}_3$ ; (a) data over the range  $0.9 \leq d/\text{\AA} \leq 3.5$  and (b)  $3 \leq d/\text{\AA} \leq 8.5$ . The refinement corresponds to structural model (1), in which all  $\text{Pb}^{2+}$  cations are located on the M1 site and all  $\text{Bi}^{3+}$  cations on the M2 site.

**Table 1. Refined Parameters for  $\text{CuPbBiS}_3$  (Space Group  $Pnma$ ) Obtained from a Rietveld Refinement Using Neutron Diffraction Data Collected at Room Temperature<sup>a</sup>**

atom	Wyckoff site	$x$	$y$	$z$	SOF	$U_{\text{iso}}$ ( $\text{\AA}^2$ )
Pb (M1)	4c	0.33288(7)	0.25	0.48930(7)	1	2.29(2)
Bi (M2)	4c	0.01707(6)	0.25	0.68216(7)	1	1.43(2)
Cu	4c	0.23464(8)	0.25	0.20908(8)	1	2.10(2)
S1	4c	0.0470(2)	0.25	0.1391(2)	1	1.28(3)
S2	4c	0.3790(2)	0.25	0.0558(2)	1	1.28(3)
S3	4c	0.2143(2)	0.25	0.8013(2)	1	1.28(3)

<sup>a</sup> $R_{\text{wp}} = 2.87\%$  and  $\text{GOF} = 2.39$ . Lattice parameters:  $a = 11.61722(7)$   $\text{\AA}$ ,  $b = 4.044072(23)$   $\text{\AA}$ , and  $c = 11.37165(7)$   $\text{\AA}$ . Weight fraction:  $\text{CuPbBiS}_3 = 98.99(5)\%$  and  $\text{PbS} = 1.01(5)\%$ .

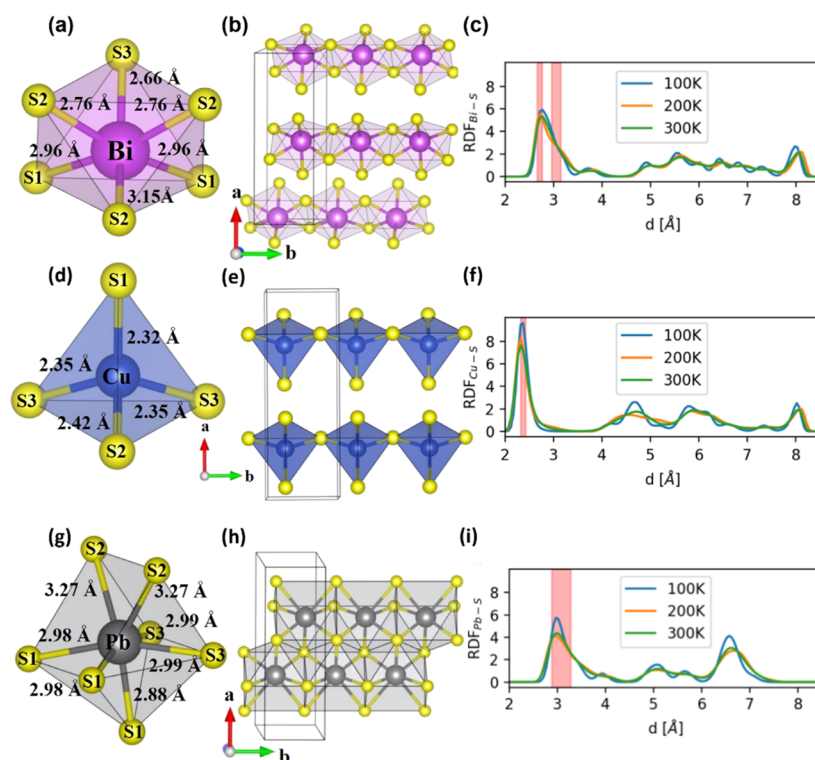


**Figure 3.** (a) Distorted octahedral coordination of  $\text{Bi}^{3+}$  (purple sphere) with sulfur (yellow sphere). (b) One-dimensional  $[\text{BiS}_4]^-$  chains directed along the  $b$ -axis. (c) Bi–S RDF computed from the  $NVT$  *ab initio* molecular dynamics trajectory. (d) Distorted tetrahedral coordination of  $\text{Cu}^+$  (blue sphere) with sulfur. (e) Chains of corner-sharing  $[\text{CuS}_4]^{7-}$  tetrahedra along the  $b$ -axis. (f) Cu–S RDF computed from the  $NVT$  *ab initio* molecular dynamics trajectory. (g) Capped octahedral coordination of  $\text{Pb}^{2+}$  (gray sphere) with sulfur. (h) Ribbons, of stoichiometry  $[\text{PbS}_3]^-$ , directed along the  $b$ -axis. (i) Pb–S RDF computed from the  $NVT$  *ab initio* molecular dynamics trajectory. Legend for the RDF plots: blue, orange, and green lines correspond to simulations at 100, 200, and 300 K, respectively; the red shaded area highlights the experimental distances.

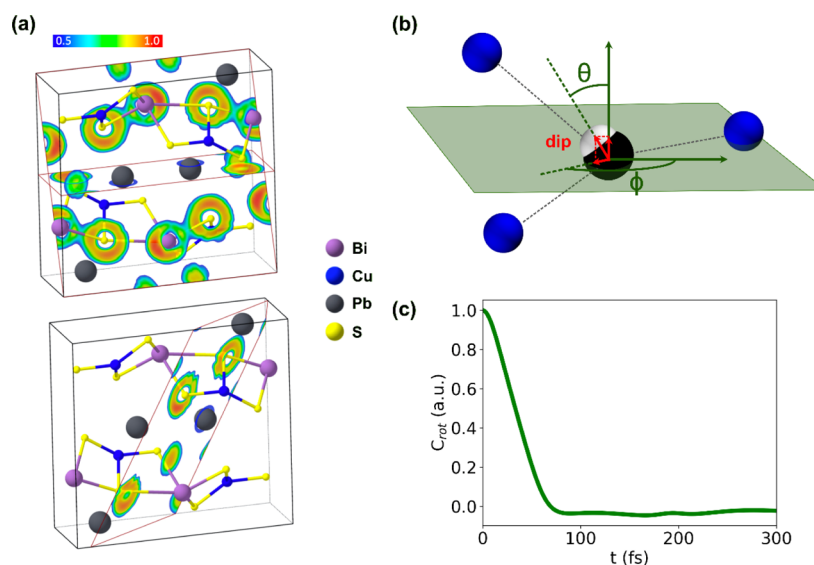


**Figure 4.** (a) Contour of the ELF on the (011) and (001) (top), and (−211) (bottom) planes. Values for the ELF range between 0 and 1: ELF = 0.5 (blue contours) indicates free electron behavior, and ELF = 1.0 (red contour) indicates perfect localization. Values smaller than 0.5 are less significant and usually point to small local electron densities. (b) *Ab initio* molecular dynamics (AIMD) snapshot highlighting the Pb<sup>2+</sup> (black)—Cu<sup>+</sup> (blue) coordination environment. The white sphere indicates the center of the maximally localized Wannier functions (MLWFC) associated with the Pb<sup>2+</sup> lone pair. The dipole moment points from the Pb<sup>2+</sup> position to the MLWFC. The  $\theta$  and  $\phi$  angles are used to indicate the dipole orientation;  $\phi$  is in the plane in which the Pb<sup>2+</sup> and one Cu<sup>+</sup> lie, and  $\theta$  is in the perpendicular plane. (c) Rotational TCF for the MLWFC dipole moment of the Pb<sup>2+</sup> lone pair.

orthorhombic unit cell (space group *Pnma*); Rietveld refinement yielded lattice parameters of  $a = 11.6136(2)$  Å,  $b = 4.0433(1)$  Å, and  $c = 11.3675(2)$  Å, which are in good agreement with those previously reported for aikinite (CuPbBiS<sub>3</sub>).<sup>60</sup> This refinement also indicates that the sample is essentially a single phase (*ca.* 99 wt %), with only trace amounts of PbS (*ca.* 1 wt %) present. Changes to the synthetic procedures, including sealed-tube synthesis instead of ball milling, different hot pressing temperatures, and replacement of elemental Pb with PbS, were attempted to remove the traces of PbS. These attempts did not increase the weight percentage of aikinite above 99%.

According to the X-ray structural model for aikinite,<sup>61</sup> in which differences in bond lengths were used to allocate crystallographic sites to bismuth and lead, the Pb<sup>2+</sup> and Bi<sup>3+</sup> cations are fully ordered into two distinct crystallographic sites, M1 (0.332, 1/4, 0.448) and M2 (0.0185, 1/4, 0.681), respectively. As it is impossible to distinguish between isoelectronic Pb<sup>2+</sup> and Bi<sup>3+</sup> by X-ray diffraction methods, we collected room-temperature powder neutron diffraction data, which provides contrast between this pair of elements ( $b_{Pb} = 9.4$ ;  $b_{Bi} = 8.5$  fm). Rietveld refinements using neutron data were carried out considering three alternative scenarios for the cation distribution: (1) all Pb<sup>2+</sup> cations located on M1 and all Bi<sup>3+</sup> cations on M2, (2) all Pb<sup>2+</sup> cations located on M2 and all Bi<sup>3+</sup> cations on M1, and (3) Pb<sup>2+</sup> and Bi<sup>3+</sup> cations disordered between the M1 and M2 sites.

Clear mismatches in intensities are observed when the Pb<sup>2+</sup> cations are located on the M2 site and the Bi<sup>3+</sup> cations are located on the M1 site (Supporting Information, Figure S2a,b), leading to a significantly higher  $R_{wp}$  factor. Structural disorder associated with the M1 and M2 sites (model (3)) was introduced by refining the site occupancy factors (SOFs), with the constraint that each site remained fully occupied and that the overall stoichiometry was maintained. This, however, did not improve  $R_{wp}$  (Supporting Information, Figure S2c,d). The lowest value of  $R_{wp}$  is found when Pb<sup>2+</sup> cations and Bi<sup>3+</sup> cations

are fully ordered on M1 and M2 sites, respectively (Figure 2). Refined parameters are presented in Table 1, while selected bond lengths and the corresponding bond valence sums are presented in the Supporting Information, Tables S1–S4. The latter are consistent with the formal oxidation states of Pb<sup>2+</sup>, Bi<sup>3+</sup>, and Cu<sup>+</sup>.

Neutron diffraction confirms that the structure of aikinite (Figure 1) contains three crystallographically distinct cation sites, which are occupied, in a fully ordered fashion, by Bi<sup>3+</sup>, Pb<sup>2+</sup>, and Cu<sup>+</sup> cations. The Bi<sup>3+</sup> cation adopts a highly distorted octahedral coordination (Figure 3a) and forms one-dimensional [BiS<sub>4</sub>]<sup>−</sup> chains of edge-sharing of [BiS<sub>6</sub>]<sup>3−</sup> octahedra, oriented parallel to the *b*-axis (Figure 3b). The highly distorted coordination of the [BiS<sub>6</sub>]<sup>3−</sup> octahedra, with three shorter and three longer Bi–S distances, arises from the displacement of the central Bi<sup>3+</sup> cation toward one of the octahedral faces. The marked polyhedral distortion is reflected in large values of the bond-angle variance<sup>62</sup> as well as non-zero values of bond-length distortion<sup>62</sup> (Supporting Information, Table S5). In the structurally related Bi<sub>2</sub>S<sub>3</sub>, the displacement of the cation from the ideal center of the octahedron has been attributed to the effect of the 6s<sup>2</sup> lone pair.<sup>63</sup> The short Bi–S distances, which vary between 2.662(2) and 2.759(2) Å, are comparable to the sum of the covalent radii<sup>64</sup> for Bi and S (*ca.* 2.53 Å). By contrast, the three longer Bi–S distances, which range between 2.962(2) and 3.145(2) Å, are larger than the sum of ionic radii for Bi<sup>3+</sup> and S<sup>2−</sup>, which is *ca.* 2.87 Å ( $r(\text{Bi}^{3+}) = 1.03$  Å and  $r(\text{S}^{2-}) = 1.84$  Å).<sup>65</sup> This indicates that the bonding environment around the Bi<sup>3+</sup> cation is heterogeneous, comprising both weaker and stronger bonds (see bond valence sums, Supporting Information Table S4). The AIMD simulations are in excellent agreement with the structural analysis: the Bi–S radial pair distribution function (RDF) obtained from NVT AIMD shows a first peak centered on the shorter bond lengths and a shoulder related to the longer Bi–S distances (Figure 3c); the asymmetry of this peak is consistent with a stereochemically active lone pair, which is evident in the electron localization function (ELF) (Figure 4). The magnitude

of the Bader charges (*vide infra*) also indicates substantial deviations from a purely ionic picture of the bonding.

The  $\text{Cu}^+$  cations adopt a distorted tetrahedral coordination (Figure 3d), with corner-sharing  $[\text{CuS}_4]^{7-}$  tetrahedra forming chains parallel to the *b*-axis (Figure 3e). The Cu–S distances vary between 2.320(2) and 2.419(2) Å, which is consistent with the computed Cu–S RDF (Figure 3f). The significant deviation of the Bader charges (*vide infra*) for  $\text{Cu}^+$  and  $\text{S}^{2-}$  from the formal oxidation states suggests a large degree of covalency for the Cu–S bonds. Each  $\text{Cu}^+$  cation is surrounded by three  $\text{Pb}^{2+}$  cations at a distance of *ca.* 3.3 Å, which is smaller than the sum of their van der Waals' radii<sup>66</sup> (*ca.* 3.8 Å) and suggests a possible interaction between the  $6s^2$  lone pairs of  $\text{Pb}^{2+}$  and the  $\text{Cu}^+$  cations. Although longer than the Pb–Cu distances, there are also Cu–Bi distances of *ca.* 3.5 and 3.7 Å, which are below the sum of the van der Waals' radii<sup>66</sup> for Bi and Cu (*ca.* 3.9 Å). These cation–cation distances are also evident in the Cu–Bi and Cu–Pb RDFs (Supporting Information, Figure S3). The  $\text{Pb}^{2+}$  cation is coordinated to seven  $\text{S}^{2-}$  anions, forming a capped octahedron (Figure 3g). Each  $[\text{PbS}_7]^{12-}$  capped octahedron shares faces with four other capped octahedra to form ribbons with stoichiometry  $[\text{PbS}_3]^-$  oriented along the *b*-axis (Figure 3h). The Pb–S distances, which range from 2.885(2) to 3.274(2) Å, are comparable to the sum of the ionic radii, which is *ca.* 3.07 Å ( $r(\text{Pb}^{2+}) = 1.23$  Å),<sup>65</sup> and in agreement with the AIMD RDF (Figure 3i). In addition, each  $\text{Pb}^{2+}$  cation has three neighboring  $\text{Cu}^+$  cations at approximately 3.3 Å (Movie S1).

Analysis of the ELF (Figure 4a), which can be used to determine if the bonding interactions involve shared electrons (e.g., covalent bonding) or unshared electrons (e.g., ionic bonding),<sup>67</sup> reveals the presence of directional covalent bonds between  $\text{Bi}^{3+}$  and  $\text{S}^{2-}$ , as well as that of a lone pair on the  $\text{Bi}^{3+}$  cations. By contrast, the distribution around the  $\text{Pb}^{2+}$  cations in the ELF contours is reasonably isotropic and spherical. This is consistent with weak electrostatic interactions between the  $\text{Pb}^{2+}$  cations and neighboring atoms, and suggests that  $\text{Pb}^{2+}$  could be considered to be in a quasi-liquid state. The isotropic ELF can arise from the dynamic behavior of the  $\text{Pb}^{2+}$  lone pair, which would give rise to rotational motion, as recently found in halide perovskites.<sup>68</sup>

The presence of different types of bonding (bond heterogeneity) has been identified as a characteristic feature that can lead to increased phonon scattering, resulting in low thermal conductivity.<sup>69–71</sup> Moreover, in agreement with a previous single-crystal X-ray diffraction study,<sup>60</sup> the atomic displacement parameters ( $U_{\text{iso}}$ ) for the  $\text{Cu}^+$  and  $\text{Pb}^{2+}$  cations are larger than those of  $\text{Bi}^{3+}$  and  $\text{S}^{2-}$  (Table 1), and the RDFs involving  $\text{Cu}^+$  and  $\text{Pb}^{2+}$  (Figures 3f,i and S3) exhibit marked peak broadening with increasing temperature. The effect of temperature has been investigated by examining the displacements of the cations with respect to their equilibrium positions (Supporting Information, Figure S4). This shows a larger response of the  $\text{Cu}^+$  and  $\text{Pb}^{2+}$  cations to increases in temperature. A large atomic displacement parameter has been related to weak interatomic bonding and “rattling”-like vibrations,<sup>19,72</sup> or to an underlying distortion at the local scale, arising from uncorrelated lone-pair stereochemical activity.<sup>73</sup> For aikinite, analysis of the AIMD trajectories performed with Wannier functions provides clear evidence of a dynamical effect arising from rotation of the  $\text{Pb}^{2+}$  lone pair (Figures 4 and Supporting Information, Figure S5 plus Movie S2). This analysis suggests that the large atomic displacement parameters for  $\text{Cu}^+$  and  $\text{Pb}^{2+}$  arise from the incoherent rotation of the  $\text{Pb}^{2+}$  lone pair,

which is accompanied by cooperative displacements of the  $\text{Pb}^{2+}$  cation toward one of the three neighboring  $\text{Cu}^+$  cations due to attractive electrostatic interaction between the lone pair and the  $\text{Cu}^+$  cation. From the statistical analysis of the AIMD trajectories, we determined the maxima of the angular amplitude for the  $\text{Pb}^{2+}$  lone pair MLWFC dipole moment; the values are  $\phi_{\text{max}} = 360^\circ$  and  $\theta_{\text{max}} = 134^\circ$ . These angles are consistent with rotation of the lone pair between the three  $\text{Cu}^+$  cations.

**Electronic Structure and Transport Properties.** Aikinite is a semiconductor with a theoretical indirect band gap of 0.8 eV (Figure 5), which is in close agreement with the indirect band

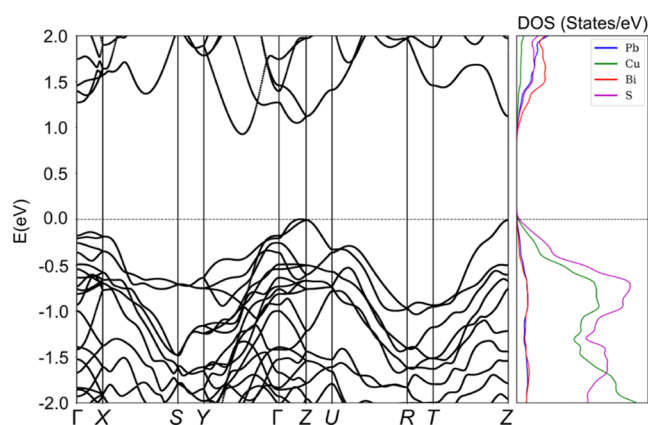


**Figure 5.** Electronic band structure (left panel) and atom-projected electron density of states (right panel) of aikinite. Spin–orbit coupling has been included in the calculation. Hubbard *U* corrections are included. The top of the valence band is set to 0 eV.

gap estimated from optical measurements, *ca.* 0.91 eV (Supporting Information, Figure S6). The computed partial density of states (Figure 5, right panel) shows that the major contribution at the top of the valence manifold arises, as expected, from the  $\text{Cu}^+$  and  $\text{S}^{2-}$  ions, which form corner-sharing tetrahedral chains. The top of the valence band has a multivalley character with large effective masses (Table S6) at the  $\Gamma$ , X, and Z high-symmetry points of the Brillouin zone (Figure 5, left panel). The effective masses, computed over the entire band structure (Table S6), are indicative of a high degree of anisotropy, which is not immediately evident from Figure 5, which shows the band structure along the high symmetry path of the Brillouin zone of aikinite. The dispersive valence band indicates significant deviation from ionic character, as demonstrated by the Bader charges, which are +1.3, +1.0, +0.5, and  $-1.0$  for Bi, Pb, Cu, and S, respectively, at  $T = 0$  K (interestingly, the values at  $T = 300$  K are +1.5/+2.0, +1.0, +1.0, and  $-1.0/-1.5$ , respectively). The features of the band structure suggest a large Seebeck coefficient for *p*-type transport, arising from the large anisotropic effective masses at Z, and the high electrical resistivity.

The conclusions from the band structure calculations are consistent with the experimentally determined Seebeck coefficient (*S*) (Figure 6a), which shows large, positive, and monotonically decreasing values between 423 and 573 K, indicating that aikinite is a nondegenerate *p*-type semiconductor. Measurements also indicate that  $\text{CuPbBiS}_3$  is highly resistive ( $1.27 \times 10^3 \Omega \text{ cm}$  at 423 K, Figure 6a), with a very low intrinsic charge carrier concentration, *ca.*  $10^{14} \text{ cm}^{-3}$ , comparable to those determined for other undoped members of the aikinite-bismuthinite series ( $4.5 \times 10^{12} \text{ cm}^{-3}$  for  $\text{CuPbBi}_5\text{S}_9$  and  $3.7 \times$



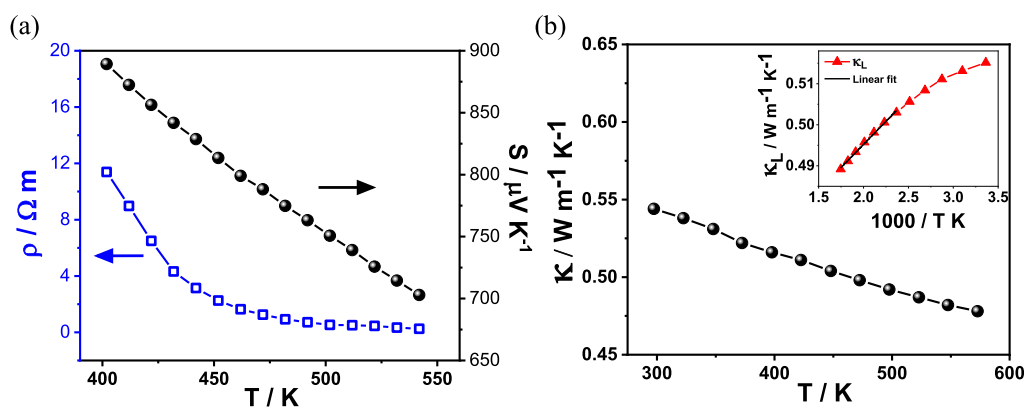


**Figure 6.** (a) Temperature dependence of the electrical resistivity ( $\rho$ ) and the Seebeck coefficient ( $S$ ) for aikinite, consistent with  $p$ -type semiconducting behavior. (b) Temperature dependence of the total thermal conductivity ( $\kappa$ ) of aikinite. The inset shows a linear fit (black line) of the lattice thermal conductivity ( $\kappa_L$ ) plotted as a function of inverse temperature.

**Table 2. Experimentally and Computationally Determined Sound Velocities and Elastic Properties Derived from the Sound Velocities for Aikinite**

	sound velocity (m s <sup>-1</sup> )			derived parameters			
	transverse $\nu_T$	longitudinal $\nu_L$	average sound velocity $\nu_a$	Poisson's ratio	Young's modulus (GPa)	Grüneisen parameter	Debye temperature $\theta_D$ (K)
Exp	1560	2771	1736	0.27	42.7	1.59	183
Th (phonon) <sup>a</sup>	1599	3123	1929	0.28		1.64	
	1865						
Th (elastic) <sup>b</sup>	1733	3199	1933	0.29		1.73	

<sup>a</sup>Determined using the phonon dispersion. <sup>b</sup>Determined using the elastic constants.

$10^{16}$  for  $\text{Bi}_2\text{S}_3$ ).<sup>29,31</sup> Unlike the intermediate composition  $\text{CuPbBi}_5\text{S}_9$  ( $x = 2/3$ ) in the bismuthinite-aikinite series  $\text{Cu}_{1-x}\text{Pb}_x\text{Bi}_{1+x}\text{S}_3$ ,<sup>31</sup> which exhibits  $n$ -type conductivity probably because of sulfur vacancies, aikinite  $\text{CuPbBiS}_3$  ( $x = 0$ ), as prepared following the synthesis route described herein, retains  $p$ -type conductivity even after repeated heated-cooling cycles (Supporting Information, Figure S7). TGA measurements (Supporting Information, Figure S8) confirm the stability of this material, which is thermally stable up to 800 K under an inert atmosphere, while DSC data are consistent with the absence of phase transitions (Supporting Information, Figure S9). While in aikinite, there is a continuous one-dimensional network of corner-sharing  $[\text{CuS}_4]^{7-}$  tetrahedra, which facilitates  $p$ -type electrical conduction, other members of the bismuthinite-aikinite series,  $\text{Cu}_{1-x}\text{Pb}_x\text{Bi}_{1+x}\text{S}_3$ , with  $x > 0$  contain vacant sites in the one-dimensional  $[\text{Cu}_{1-x}\text{Pb}_x\text{S}_3]^{(5+x)-}$  chains instead of a continuous network. Therefore, in copper-deficient materials, such as  $\text{CuPbBi}_5\text{S}_9$ ,  $n$ -type electrical conduction involves the Bi–S network, as previously discussed by Maji *et al.*<sup>31</sup>

A study of the formation of defects in  $\text{Bi}_2\text{S}_3$  ( $x = 1$ ) has shown that for the S rich limit, Bi vacancies ( $\square_{\text{Bi}}^{\text{III}}$ ) and S antisite defects ( $\text{S}_{\text{Bi}}^{\text{III}}$ ) are dominant, while in the Bi rich limit, the dominant defects are S vacancies ( $\square_{\text{S}}^{\text{II}}$ ) and Bi antisite defects ( $\text{Bi}_{\text{S}}^{\text{III}}$ ).<sup>74</sup> The situation for  $\text{CuPbBiS}_3$  is more complex. Acceptor defects that can occur in aikinite include copper vacancies ( $\square_{\text{Cu}}^{\text{II}}$ ) usually observed in chalcogenides, lead vacancies ( $\square_{\text{Pb}}^{\text{II}}$ ), antisite defects of Cu at the Pb site ( $\text{Cu}_{\text{Pb}}^{\text{II}}$ ) or Pb on the Bi site ( $\text{Pb}_{\text{Bi}}^{\text{II}}$ ). In addition, bismuth vacancies ( $\square_{\text{Bi}}^{\text{III}}$ ), owing to the volatility of bismuth, could also form, although under the synthesis conditions (low temperature annealing and hot-pressing) used here, this is considered unlikely. A detailed study of the energetics of defect formation is ongoing.

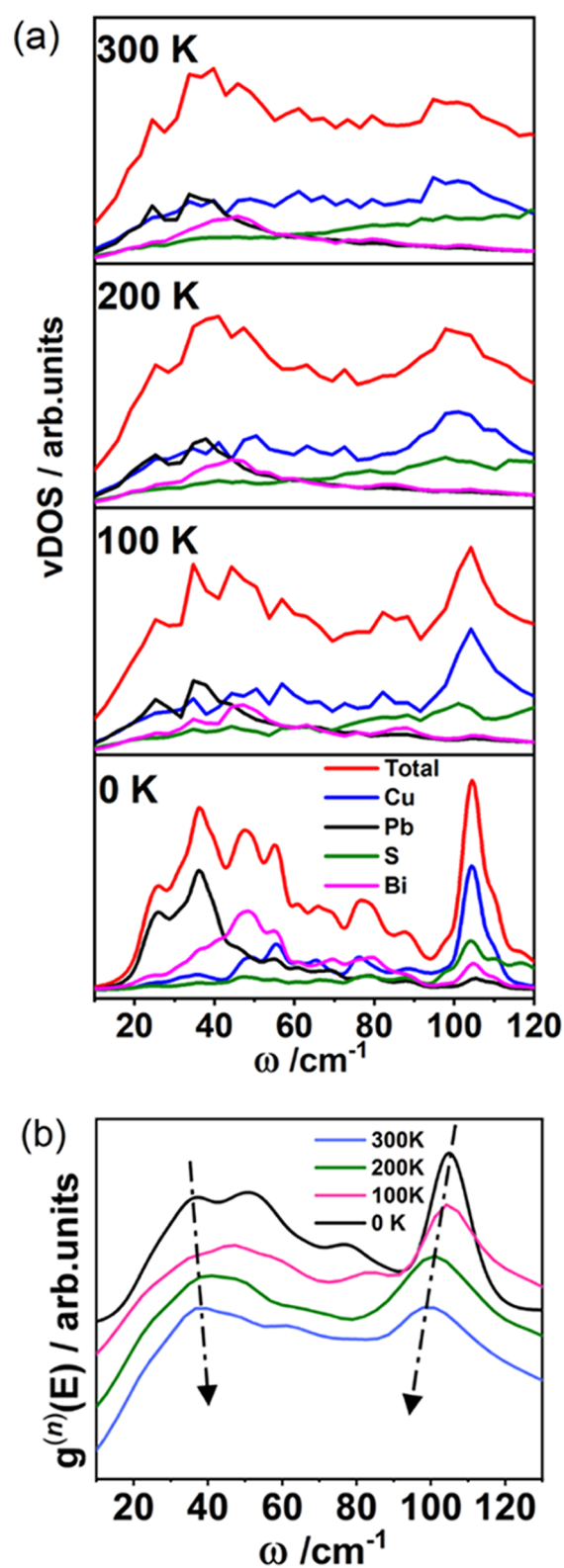
**Lattice Thermal Conductivity and Elastic and Vibrational Properties.** The total thermal conductivity of  $\text{CuPbBiS}_3$  (Figure 6b) is extremely low ( $\sim 0.5 \text{ W m}^{-1} \text{ K}^{-1}$ ) and is dominated by the lattice component,  $\kappa_L$  (Supporting Information, Figure S10a), which constitutes approximately 99% of the total thermal conductivity.  $\kappa_L$  follows a  $T^{-1}$  law only at temperatures above 450 K, indicating a significant contribution from Umklapp type scattering above this temperature (Figure 6b, inset). Despite the differences in cation ordering between  $\text{CuPbBi}_5\text{S}_9$ , in which there is disorder between  $\text{Cu}^+$  and vacancies on the copper site and between  $\text{Pb}^{2+}$  and  $\text{Bi}^{3+}$  cations on the M1 site,<sup>31</sup> and  $\text{CuPbBiS}_3$ , in which  $\text{Cu}^+$ ,  $\text{Pb}^{2+}$ , and  $\text{Bi}^{3+}$  cations are fully ordered, the thermal conductivities of  $\text{CuPbBiS}_3$  and  $\text{CuPbBi}_5\text{S}_9$  are very similar. By contrast,  $\text{Bi}_2\text{S}_3$  ( $x = 1$ ) exhibits significantly larger thermal conductivities; for highly oriented ingots, the thermal conductivity is  $\sim 1.3 \text{ W m}^{-1} \text{ K}^{-1}$  along the  $b$ -axis and  $\sim 0.9 \text{ W m}^{-1} \text{ K}^{-1}$  along  $a$  and  $c$ ,<sup>29</sup> while polycrystalline  $\text{Bi}_2\text{S}_3$  exhibits a total thermal conductivity of  $\sim 0.87 \text{ W m}^{-1} \text{ K}^{-1}$  at room temperature.<sup>74</sup> Therefore, the reduction in thermal conductivity that occurs in  $\text{Cu}_{1-x}\text{Pb}_x\text{Bi}_{1+x}\text{S}_3$  for  $x < 1$  suggests that  $\text{Cu}^+$  and  $\text{Pb}^{2+}$  cations play a key role in the heat transport. To investigate the origin of the ultralow thermal conductivity in aikinite, sound velocity measurements were performed, from which elastic properties were derived (Table S7). The sound velocities obtained computationally are in good agreement with the experimental values (Table 2). Both the transverse ( $1560 \text{ m s}^{-1}$ ) and the longitudinal sound velocities ( $2771 \text{ m s}^{-1}$ ), which can be related to the group velocities of the heat-carrying acoustic phonons, are low and comparable to those for  $\text{CuPbBi}_5\text{S}_9$  ( $x = 2/3$ ).<sup>31,32</sup> Since it has been shown<sup>75</sup> that, above the Debye temperature,  $\kappa_L$  is directly proportional to the cube of the average sound velocity ( $\kappa_L = A\nu_a^3/T$ , where  $A$  is a proportion-

ality constant), a low sound velocity is expected to result in low thermal conductivity. For aikinite, the minimum value of  $\kappa_L$ , according to the Cahill-Watson-Pohl (CWP) model,<sup>37</sup> which describes the limit for amorphous and strongly disordered materials, is *ca.*  $0.41 \text{ W m}^{-1} \text{ K}^{-1}$ . This is similar to the experimental value of 0.48 at 573 K determined here. The minimum  $\kappa_L$  can also be calculated by considering a diffusive mechanism in which nonpropagating (i.e., not phononic) atomic vibrations, known as diffusons, carry heat by diffusion.<sup>76</sup> This leads to an estimate of the diffuson thermal conductivity,  $\kappa_{\text{diff}} \sim 0.26 \text{ W m}^{-1} \text{ K}^{-1}$ . This represents the limit for entirely diffusive mediated transport and is significantly lower than the values found for aikinite, providing a strong indicator that phonons contribute to heat transport in aikinite. Taking into account that  $\kappa_L = 1/3 C_p v_a l$  (where  $C_p$  is the heat capacity per unit volume, and  $l$  is the phonon mean-free-path), the estimated phonon mean-free-path is *ca.*  $5 \text{ \AA}$ , which is approximately twice the interatomic spacing in aikinite and comparable to the  $b$  lattice parameter.

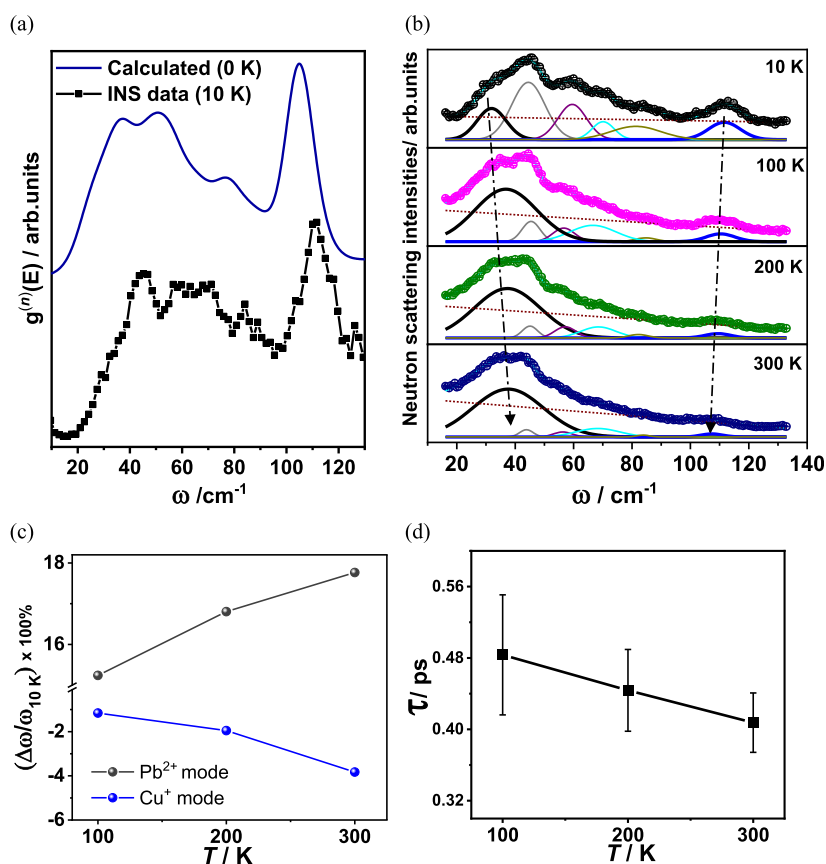
The Grüneisen parameter derived from the sound velocity measurements is large,  $\gamma \sim 1.59$ , indicating a high degree of anharmonicity and comparable to values found for other thermoelectric materials with low thermal conductivities (Supporting Information, Table S8). The Grüneisen parameter obtained here is similar to that reported for other members of the  $\text{Cu}_{1-x}\text{Pb}_x\text{Bi}_{1+x}\text{S}_3$  series (Supporting Information, Table S9). Anharmonicity enhances phonon–phonon scattering processes, hence lowering the lattice thermal conductivity. The Young's modulus ( $E$ ), extracted from the sound velocities (Table 2), is rather low (Supporting Information, Table S8), and similar to values reported for other members of the  $\text{Cu}_{1-x}\text{Pb}_x\text{Bi}_{1+x}\text{S}_3$  series (Supporting Information, Table S9). As the Young's modulus is related to the stiffness of the atomic bonds, this is indicative of weaker interatomic bonding. This supports the conclusions drawn from the structural analysis.

Figure 7 presents the atom-resolved phonon density of states (vDOS) computed at 100, 200, and 300 K by AIMD, compared with the vDOS at 0 K<sup>31</sup> calculated using Quantum ESPRESSO. These results should also be compared with the dispersion curves presented in ref 31, which show optical modes with very low frequencies ( $\sim 20\text{--}50 \text{ cm}^{-1}$ ). It has been shown that a low cutoff frequency of acoustic phonons, which can be ascribed to weak bonding and a correspondingly low sound velocity, is a good indicator for low thermal conductivity.<sup>77</sup> Moreover, the presence of low-frequency optical modes close to the acoustic mode frequencies, as is the case here, can lead to phonon scattering and affect thermal transport.

Low-frequency optical modes in the range  $20\text{--}50 \text{ cm}^{-1}$  and Einstein-like modes centered around  $100 \text{ cm}^{-1}$  are evident in the vDOS of aikinite (Figure 7). The atom-resolved vDOS shows that the main contribution at low frequencies is from  $\text{Pb}^{2+}$ , with a smaller contribution from  $\text{Bi}^{3+}$ . It is interesting to note that the difference between the  $\text{Bi}^{3+}$  and  $\text{Pb}^{2+}$  modes at low frequencies cannot be accounted for in terms of the variation in atomic mass (208.9 and 207.2 amu, respectively), but is consistent with the weak bonding of  $\text{Pb}^{2+}$  highlighted by the structural analysis. In addition, analysis of the vDOS computed by AIMD as a function of temperature (Figure 7a) indicates that, with increasing temperature, the  $\text{Cu}^+$  vibrational modes spread and shift to lower frequencies, overlapping more with phonons with a large  $\text{Pb}^{2+}$  component, while the  $\text{Bi}^{3+}$  contribution remains largely unchanged (Figure 7a). The shift, with increasing temperature,



**Figure 7.** (a) Total (red line) and atom-resolved vDOS of aikinite at different temperatures. Blue, black, green, and purple lines correspond to  $\text{Cu}^+$ ,  $\text{Pb}^{2+}$ ,  $\text{S}^{2-}$ , and  $\text{Bi}^{3+}$  ions, respectively. The vDOS at 0 K was computed using Quantum ESPRESSO and those between 100 and 300 K by AIMD. (b) Neutron-weighted total vDOS calculated with the LET instrumental resolution function as a function of temperature. Arrows indicate shifts in peak positions.



**Figure 8.** (a) Calculated neutron-weighted total vDOS ( $g^n(E)$ ) (convolved with the instrumental resolution) at 0 K (blue line) and experimental neutron-weighted vDOS (black) at 10 K. Data have been normalized. (b) Neutron scattering intensities as a function of temperature. Gaussian fits for the six peaks are shown. The Gaussian corresponding to the  $\text{Pb}^{2+}$ -based vibration is shown as a black line, and that for the  $\text{Cu}^+$  rattling vibration is shown as a blue line. Experimental data have been offset along the y axis with respect to the Gaussian fits for clarity. The red dotted line shows the fitted background. Arrows highlight the change in peak position for the  $\text{Pb}^{2+}$ -based and  $\text{Cu}^+$  rattling vibrations with temperature. (c) Percentage change in the energy of the phonon mode between 10 K and a temperature  $T$ . The gray line corresponds to the  $\text{Pb}^{2+}$  mode ( $\omega = 32 \text{ cm}^{-1}$ ) and the blue line corresponds to the  $\text{Cu}^+$  mode ( $\omega = 110 \text{ cm}^{-1}$ ). (d) Temperature dependence of the phonon lifetime of the  $\text{Pb}^{2+}$  mode.

of the  $\text{Cu}^+$  vibrational modes to lower frequencies and of the peak at *ca.*  $31 \text{ cm}^{-1}$  toward higher frequencies is also evident in the neutron-weighted total calculated vDOS convolved with the LET instrumental resolution function (Figure 7b).

In order to confirm, experimentally, the presence of the low-energy phonon modes of  $\text{Pb}^{2+}$  and the Einstein-like modes arising from the  $\text{Cu}^+$  vibrations described above, temperature-dependent INS data were collected. The calculated neutron-weighted vDOS (convolved with a Gaussian function approximating the instrumental resolution) and the experimental vDOS are in very good agreement (Figure 8a and Supporting Information, Figure S11). The slight shift in frequencies between the experimental and calculated vDOS is due to the PBE functional used in the calculations, which is known to underestimate bond strengths, and the slight differences in peak intensities are related to approximations made when convolving the INS instrumental resolution with the calculated vDOS. A comparison with the partial calculated vDOS (Figure 7a) allows us to assign the first peak in the experimental vDOS, which at 10 K is centered at  $31.7 \text{ cm}^{-1}$ , to primarily  $\text{Pb}^{2+}$ -based vibrations. Of the other five peaks present in the INS data, most have contributions from multiple atoms, and only that at  $110.7 \text{ cm}^{-1}$  can be assigned to the Einstein-like modes of  $\text{Cu}^+$ . Examination of the experimental vDOS collected as a function of temperature (Figure 8b) shows that peaks shift significantly with temperature (Table S10). In particular, with

increasing temperature (Figure 8c), the  $\text{Cu}^+$  mode softens, in agreement with the findings of the computed vDOS. By contrast, the phonon peak corresponding to the  $\text{Pb}^{2+}$ -based mode shifts to a higher frequency (Figure 8c). Such “hardening” of the  $\text{Pb}^{2+}$  mode with increasing temperature is indicative of anharmonic behavior and is therefore likely to be a key contributor to the ultralow thermal conductivity of aikinite. To evaluate the role of  $\text{Pb}^{2+}$  in lowering the lattice thermal conductivity, we used the quasi-harmonic approximation to estimate the degree of anharmonicity through the mode-resolved Grüneisen parameter,  $\gamma_{i\omega}$  and its atom projection as a function of the frequency (Figure 9). This analysis provides clear evidence for significant anharmonicity. While in aikinite, anharmonicity could be associated with the presence of the  $6s^2$  lone pair of electrons found in  $\text{Pb}^{2+}$  and  $\text{Bi}^{3+}$  cations, examination of Figure 9 reveals that at low frequencies, over the range  $20\text{--}50 \text{ cm}^{-1}$ , the magnitude of mode-resolved Grüneisen parameter is significantly higher for  $\text{Pb}^{2+}$  than for the other atoms. Finally, the rotational TCF (Figure 4c) associated with the  $\text{Pb}^{2+}$  lone pair shows a rotational time scale of  $\sim 80 \text{ fs}$ ; this corresponds to a frequency of  $\sim 66 \text{ cm}^{-1}$ , comparable with the low-frequency mode of  $\text{Cu}^+$ . This observation is consistent with the cooperative interaction between the rotation of the  $\text{Pb}^{2+}$  lone pair and the  $\text{Cu}^+$  cations discussed earlier.

Other members of the bismuthinite-aikinite series,  $\text{Cu}_{1-x}\square_x\text{Pb}_{1-x}\text{Bi}_{1+x}\text{S}_3$ , are isostructural with aikinite ( $x = 0$ ),

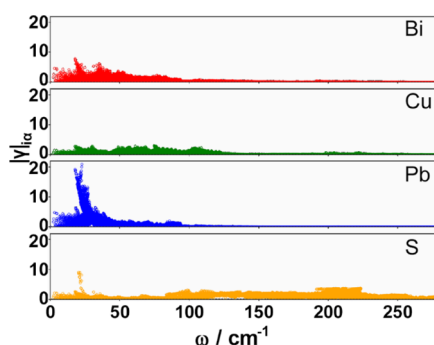


**Figure 9.** Contribution of each atomic species to the total Grüneisen parameter as a function of the mode frequency. Red, green, blue, and yellow points correspond to  $\text{Bi}^{3+}$ ,  $\text{Cu}^+$ ,  $\text{Pb}^{2+}$ , and  $\text{S}^{2-}$  contributions, respectively.

and when  $x < 1$ , also contain  $\text{Cu}^+$  and  $\text{Pb}^{2+}$  cations at relatively short distances, which could facilitate coupling of rotating lone pairs and the vibrational motion of the  $\text{Cu}^+$  cations. Moreover, based on the limited data available in the literature, members of this series with  $x < 1$  exhibit similarly low values of thermal conductivity to those of aikinite. This ultralow thermal conductivity has previously been ascribed to the complex crystal structure with a large unit cell and heavy atoms,<sup>32</sup> or to disorder.<sup>78</sup> However, given that aikinite has an ultralow thermal conductivity even with complete ordering of the  $\text{Cu}^+$ ,  $\text{Pb}^{2+}$ , and  $\text{Bi}^{3+}$  cations, we can effectively discount disorder as the origin of the ultralow thermal conductivity in other members of the  $\text{Cu}_{1-x}\text{Pb}_x\text{Bi}_{1+x}\text{S}_3$  series with  $x < 1$ . Furthermore, the larger thermal conductivity of  $\text{Bi}_2\text{S}_3$  ( $x = 1$ ) when compared to other members of the series indicates that the  $\text{Cu}^+$  and  $\text{Pb}^{2+}$  cations play a key role in heat transport. Together, these observations suggest that the mechanism of lone pair rotation we have unveiled in aikinite, which we have demonstrated is a key contributor to the scattering effects that lower the thermal conductivity, is also at play in other members of the bismuthinite-aikinite series,  $\text{Cu}_{1-x}\text{Pb}_x\text{Bi}_{1+x}\text{S}_3$ .

It is extremely challenging to extract lifetimes from INS data collected on a powder, owing to the averaging over Brillouin zones that occurs in such an experiment.<sup>69</sup> This is especially true when, with increasing temperature, modes are shifting very significantly in frequency and in different directions, with corresponding changes to the underlying dispersion. As a result, peaks might sharpen or broaden independent of broadening from phonon–phonon scattering. In the INS data for aikinite, the full width at half maxima (FWHM) of the majority of the peaks decreases with increasing temperature (Supporting Information Table S11), indicating that the modes sharpen at higher temperatures. Such a sharpening could be related to a flattening of the dispersion and, thereby, a reduction in the optical mode group velocities. However, for  $\text{Pb}^{2+}$ , the low-energy mode broadens with increasing temperature (Table 3 and Supporting Information Table S11). While it is not possible to disentangle the likely changes to the dispersion from phonon–phonon scattering, if we assume that the broadening is all from phonon–phonon scattering, we can extract a rather low lifetime of 0.41(3) ps at 300 K (Table 3 and Figure 8d). This compares favorably with the values of  $\sim 3$  ps,  $\sim 0.66$  ps and  $\sim 2$  ps for  $\text{PbTe}$ ,<sup>79</sup>  $\text{TlInTe}_2$ <sup>69</sup> or  $\text{Na}_{0.8}\text{CoO}_2$ ,<sup>80</sup> respectively. While the lifetime determined here should be considered a lower bound, since it is likely that at least some of the broadening is due to changes in the dispersion, this lifetime would correspond to a phonon

**Table 3. Phonon Lifetime ( $\tau$ ) for the  $\text{Pb}^{2+}$  Mode<sup>a</sup>**

$T$ (K)	peak center ( $\text{cm}^{-1}$ )	FWHM ( $\text{cm}^{-1}$ )	$\Delta_{\text{FWHM}}$ ( $\text{cm}^{-1}$ )	$\tau$ (ps)
10	31.7(4)	11.6(5)		
100	36.5(4)	24.7(8)	21.7(4)	0.48(7)
200	36.9(3)	26.4(5)	23.7(3)	0.44(5)
300	37.3(2)	28.3(4)	25.8(3)	0.41(3)

<sup>a</sup>Calculated using the relation<sup>69,81</sup>

$$\tau = \frac{1}{\pi(\Delta_{\text{FWHM}})}$$

$$\text{where } \Delta_{\text{FWHM}} = \sqrt{(\text{FWHM}_T)^2 - (\text{FWHM}_{10\text{K}})^2}$$

mean-free-path ( $l = v_a \tau$ ) of *ca.* 7 Å, which is in reasonable agreement with the estimated mean-free-path based on the lattice thermal conductivity.

## CONCLUSIONS

In aikinite, the combination of bond heterogeneity and the presence of heavy-metal cations with stereochemically-active lone pairs leads to an exceptionally low thermal conductivity. Moreover, the  $\text{Cu}^+$  and  $\text{Pb}^{2+}$  cations have large atomic displacement parameters and contribute to the same low-frequency vibrational manifold. With increasing temperature, the  $\text{Cu}^+$  contributions in the low-frequency region increase. This is consistent with a thermally activated interaction between  $\text{Cu}^+$  and  $\text{Pb}^{2+}$  cations. Using *ab-initio* molecular dynamics and Wannier function analysis, we have characterized the weak and isotropic bonding of the  $\text{Pb}^{2+}$  cations that facilitates the rotation of the  $6s^2$  lone pair. In turn, such rotations influence the  $\text{Cu}^+$  dynamics and reduce the thermal conductivity. The interaction mechanism can be rationalized by considering the electrostatic attraction between the thermally activated lone pairs on the  $\text{Pb}^{2+}$  cations, which are rotating, and the  $\text{Cu}^+$  cations. Given that synthetic samples in the bismuthinite-aikinite series,  $\text{Cu}_{1-x}\text{Pb}_x\text{Bi}_{1+x}\text{S}_3$ , are isostructural with aikinite ( $x = 0$ ), it is highly likely that the ultralow thermal conductivity observed for this family of materials is also a consequence of the cooperative interaction between the rotating lone pair on the  $\text{Pb}^{2+}$  cations and the  $\text{Cu}^+$  cations.

Lone pair rotation in solids is an emergent phenomenon, recently reported in halide perovskites, although it has been suggested that such rotational motion may also occur in other solids containing lone-pair electrons.<sup>57</sup> The work presented here provides clear evidence for the dynamical behavior of the  $\text{Pb}^{2+}$  lone pair and its contribution to lowering thermal conductivity, in a family of thermoelectric sulfides,  $\text{Cu}_{1-x}\text{Pb}_x\text{Bi}_{1+x}\text{S}_3$ . We have demonstrated, for the first time, that the coupling of rotating lone pairs with vibrational motion is an effective mechanism to achieve ultralow thermal conductivity in crystalline materials. We suggest that this mechanism may also occur in other families of materials, including halide perovskites such as  $\text{CsSnBr}_{3-x}\text{I}_x$ , which also exhibit ultralow thermal conductivities.<sup>82</sup> Therefore, the results presented here offer new insights for the search for materials with ultralow thermal conductivity.

## ASSOCIATED CONTENT

### Supporting Information

The Supporting Information is available free of charge at <https://pubs.acs.org/doi/10.1021/jacs.3c02536>.

Details of the methodology, Helmholtz free energy, internal energy, entropy and specific heat, Rietveld refinements using different models, bond distances, bond valence sums and distortion parameters, RDF plots, ion displacement plots, diffuse reflectance, TGA, DSC, heat capacity, electrical and thermal transport data, calculated effective masses, computed vibrational DOS determined using INS data and derived parameters, and computed elastic constants (PDF)

Vibrations of  $\text{Pb}^{2+}$  (black sphere) and  $\text{Cu}^+$  (blue sphere), with distances shown (MP4)

AIMD showing the  $\text{Pb}^{2+}$  lone pair rotation (MP4)

## AUTHOR INFORMATION

### Corresponding Authors

**Paz Vaqueiro** – Department of Chemistry, University of Reading, Reading RG6 6DX, U.K.; [orcid.org/0000-0001-7545-6262](https://orcid.org/0000-0001-7545-6262); Email: [p.vaqueiro@reading.ac.uk](mailto:p.vaqueiro@reading.ac.uk)

**Marco Fornari** – Department of Physics and Science of Advanced Materials Program, Central Michigan University, Mt. Pleasant, Michigan 48859, United States; [orcid.org/0000-0001-6527-8511](https://orcid.org/0000-0001-6527-8511); Email: [marco.fornari@cmich.edu](mailto:marco.fornari@cmich.edu)

### Authors

**Virginia Carnevali** – Department of Physics and Science of Advanced Materials Program, Central Michigan University, Mt. Pleasant, Michigan 48859, United States; Present Address: Laboratory of Computational Chemistry and Biochemistry, École Polytechnique Fédérale de Lausanne, 1015 Lausanne, Switzerland; [orcid.org/0000-0002-8905-2928](https://orcid.org/0000-0002-8905-2928)

**Shriparna Mukherjee** – Department of Chemistry, University of Reading, Reading RG6 6DX, U.K.; [orcid.org/0000-0002-1941-5551](https://orcid.org/0000-0002-1941-5551)

**David J. Voneshen** – ISIS Pulsed Neutron and Muon Source, Rutherford Appleton Laboratory, Didcot OX11 0QX, U.K.; Department of Physics, Royal Holloway University of London, Egham TW20 0EX, U.K.

**Krishnendu Maji** – CRISMAT, CNRS, Normandie Univ, ENSICAEN, UNICAEN, Caen 14000, France

**Emmanuel Guilmeau** – CRISMAT, CNRS, Normandie Univ, ENSICAEN, UNICAEN, Caen 14000, France; [orcid.org/0000-0001-7439-088X](https://orcid.org/0000-0001-7439-088X)

**Anthony V. Powell** – Department of Chemistry, University of Reading, Reading RG6 6DX, U.K.; [orcid.org/0000-0002-9650-1568](https://orcid.org/0000-0002-9650-1568)

Complete contact information is available at: <https://pubs.acs.org/10.1021/jacs.3c02536>

### Author Contributions

<sup>†</sup>V.C. and S.M. contributed equally to this work.

### Notes

The authors declare no competing financial interest.

## ACKNOWLEDGMENTS

The authors acknowledge the Leverhulme Trust for Research Project Grant RPG-2019-288, which funded this work. We would also like to acknowledge the STFC ISIS Neutron and Muon Source for the provision of beam time on the LET beamline under proposal RB2210076. This research used resources at the Spallation Neutron Source (experiment IPTS-29028.1), a DOE Office of Science User Facility operated by the

Oak Ridge National Laboratory. We also thank the Chemical Analysis Facility (CAF) at the University of Reading, Reading, UK, for access to powder X-ray diffraction and thermal analysis instrumentation. Calculations were performed at the High-Performance Computing Center at Michigan State University. We thank Rajendra Paudel for useful discussions.

## REFERENCES

- (1) Padture, N. P.; Gell, M.; Jordan, E. H. Thermal Barrier Coatings for Gas-Turbine Engine Applications. *Science* **2002**, *296*, 280–284.
- (2) Wang, Q.; Jiang, B.; Li, B.; Yan, Y. A Critical Review of Thermal Management Models and Solutions of Lithium-Ion Batteries for the Development of Pure Electric Vehicles. *Renew. Sustain. Energy Rev.* **2016**, *64*, 106–128.
- (3) Ghosh, T.; Dutta, M.; Sarkar, D.; Biswas, K. Insights into Low Thermal Conductivity in Inorganic Materials for Thermoelectrics. *J. Am. Chem. Soc.* **2022**, *144*, 10099–10118.
- (4) Biswas, K.; He, J.; Blum, I. D.; Wu, C.-I.; Hogan, T. P.; Seidman, D. N.; Dravid, V. P.; Kanatzidis, M. G. High-Performance Bulk Thermoelectrics with All-Scale Hierarchical Architectures. *Nature* **2012**, *489*, 414–418.
- (5) Kim, S. I.; Lee, K. H.; Mun, H. A.; Kim, H. S.; Hwang, S. W.; Roh, J. W.; Yang, D. J.; Shin, W. H.; Li, X. S.; Lee, Y. H.; Snyder, G. J.; Kim, S. W. Dense Dislocation Arrays Embedded in Grain Boundaries for High-Performance Bulk Thermoelectrics. *Science* **2015**, *348*, 109–114.
- (6) Hsu, K. F.; Loo, S.; Guo, F.; Chen, W.; Dyck, J. S.; Uher, C.; Hogan, T.; Polychroniadis, E. K.; Kanatzidis, M. G. Cubic  $\text{AgPb}_m\text{SbTe}_{2+m}$ : Bulk Thermoelectric Materials with High Figure of Merit. *Science* **2004**, *303*, 818–821.
- (7) Suekuni, K.; Kim, F. S.; Nishiate, H.; Ohta, M.; Tanaka, H. I.; Takabatake, T. High-Performance Thermoelectric Minerals: Colusites  $\text{Cu}_{26}\text{V}_2\text{M}_6\text{S}_{32}$  (M = Ge, Sn). *Appl. Phys. Lett.* **2014**, *105*, 132107.
- (8) Kumar, V. P.; Lemoine, P.; Carnevali, V.; Guérou, G.; Lebedev, O. I.; Raveau, B.; Al Rahal Al Orabi, R.; Fornari, M.; Candolfi, C.; Prestipino, C.; Menut, D.; Malaman, B.; Juraszek, J.; Suekuni, K.; Guilmeau, E. Local-Disorder-Induced Low Thermal Conductivity in Degenerate Semiconductor  $\text{Cu}_{22}\text{Sn}_{10}\text{S}_{32}$ . *Inorg. Chem.* **2021**, *60*, 16273–16285.
- (9) Guérou, G.; Pavan Kumar, V.; Carnevali, V.; Lebedev, O. I.; Raveau, B.; Couder, C.; Prestipino, C.; Lemoine, P.; Malaman, B.; Juraszek, J.; Candolfi, C.; Lenoir, B.; Al Rahal Al Orabi, R.; Fornari, M.; Guilmeau, E. Long-Range Cationic Order Collapse Triggered by S/Cl Mixed-Anion Occupancy Yields Enhanced Thermoelectric Properties in  $\text{Cu}_5\text{Sn}_2\text{S}_7$ . *Chem. Mater.* **2021**, *33*, 9425–9438.
- (10) Liu, H.; Shi, X.; Xu, F.; Zhang, L.; Zhang, W.; Chen, L.; Li, Q.; Uher, C.; Day, T.; Snyder, G. J. Copper Ion Liquid-like Thermoelectrics. *Nat. Mater.* **2012**, *11*, 422–425.
- (11) Lai, W.; Wang, Y.; Morelli, D. T.; Lu, X. From Bonding Asymmetry to Anharmonic Rattling in  $\text{Cu}_{12}\text{Sb}_4\text{S}_{13}$  Tetrahedrites: When Lone-Pair Electrons Are Not So Lonely. *Adv. Funct. Mater.* **2015**, *25*, 3648–3657.
- (12) Lee, S.; Esfarjani, K.; Luo, T.; Zhou, J.; Tian, Z.; Chen, G. Resonant Bonding Leads to Low Lattice Thermal Conductivity. *Nat. Commun.* **2014**, *5*, 3525.
- (13) Nielsen, M. D.; Ozolins, V.; Heremans, J. P. Lone Pair Electrons Minimize Lattice Thermal Conductivity. *Energy Environ. Sci.* **2013**, *6*, 570–578.
- (14) Sato, N.; Kuroda, N.; Nakamura, S.; Katsura, Y.; Kanazawa, I.; Kimura, K.; Mori, T. Bonding Heterogeneity in Mixed-Anion Compounds Realizes Ultralow Lattice Thermal Conductivity. *J. Mater. Chem. A* **2021**, *9*, 22660–22669.
- (15) Dutta, M.; Pal, K.; Waghmare, U. V.; Biswas, K.; Biswas, K. Bonding Heterogeneity and Lone Pair Induced Anharmonicity Resulted in Ultralow Thermal Conductivity and Promising Thermoelectric Properties in N-Type  $\text{AgPbBiSe}_3$ . *Chem. Sci.* **2019**, *10*, 4905–4913.

- (16) Vaqueiro, P. Synthesis and Property Measurements of Thermoelectric Materials. *Inorganic Thermoelectric Materials*; Royal Society of Chemistry: 2021; pp 1–52, Chapter 1.
- (17) Powell, A. V. Recent Developments in Earth-Abundant Copper-Sulfide Thermoelectric Materials. *J. Appl. Phys.* **2019**, *126*, 100901.
- (18) Vaqueiro, P.; Guérou, G.; Kaltzoglou, A.; Smith, R. I.; Barbier, T.; Guilmeau, E.; Powell, A. V. The Influence of Mobile Copper Ions on the Glass-Like Thermal Conductivity of Copper-Rich Tetrahedrites. *Chem. Mater.* **2017**, *29*, 4080–4090.
- (19) Long, S. O.; Powell, A. V.; Hull, S.; Orlandi, F.; Tang, C. C.; Supka, A. R.; Fornari, M.; Vaqueiro, P. Jahn–Teller Driven Electronic Instability in Thermoelectric Tetrahedrite. *Adv. Funct. Mater.* **2020**, *30*, 1909409.
- (20) Suekuni, K.; Tsuruta, K.; Kunii, M.; Nishiata, H.; Nishibori, E.; Maki, S.; Ohta, M.; Yamamoto, A.; Koyano, M. High-Performance Thermoelectric Mineral  $\text{Cu}_{12-x}\text{Ni}_x\text{Sb}_4\text{S}_{13}$  Tetrahedrite. *J. Appl. Phys.* **2013**, *113*, 043712.
- (21) Lu, X.; Morelli, D. T.; Xia, Y.; Zhou, F.; Ozolins, V.; Chi, H.; Zhou, X.; Uher, C. High Performance Thermoelectricity in Earth-Abundant Compounds Based on Natural Mineral Tetrahedrites. *Adv. Energy Mater.* **2013**, *3*, 342–348.
- (22) Barbier, T.; Lemoine, P.; Gascoin, S.; Lebedev, O. I.; Kaltzoglou, A.; Vaqueiro, P.; Powell, A. V.; Smith, R. I.; Guilmeau, E. Structural Stability of the Synthetic Thermoelectric Ternary and Nickel-Substituted Tetrahedrite Phases. *J. Alloys Compd.* **2015**, *634*, 253–262.
- (23) Bourges, C.; Bouyrie, Y.; Supka, A. R.; Al Rahal Al Orabi, R.; Lemoine, P.; Lebedev, O. I.; Ohta, M.; Suekuni, K.; Nassif, V.; Hardy, V.; Daou, R.; Miyazaki, Y.; Fornari, M.; Guilmeau, E. High-Performance Thermoelectric Bulk Colusite by Process Controlled Structural Disorder. *J. Am. Chem. Soc.* **2018**, *140*, 2186–2195.
- (24) Pavan Kumar, V.; Guérou, G.; Lemoine, P.; Raveau, B.; Supka, A. R.; Al Rahal Al Orabi, R.; Fornari, M.; Suekuni, K.; Guilmeau, E. Copper-Rich Thermoelectric Sulfides: Size-Mismatch Effect and Chemical Disorder in the  $[\text{TS}_4]\text{Cu}_6$  Complexes of  $\text{Cu}_{26}\text{T}_2\text{Ge}_6\text{S}_{32}$  (T = Cr, Mo, W) Colusites. *Angew. Chem., Int. Ed.* **2019**, *58*, 15455–15463.
- (25) Pavan Kumar, V.; Supka, A. R.; Lemoine, P.; Lebedev, O. I.; Raveau, B.; Suekuni, K.; Nassif, V.; Al Rahal Al Orabi, R.; Fornari, M.; Guilmeau, E. High Power Factors of Thermoelectric Colusites  $\text{Cu}_{26}\text{T}_2\text{Ge}_6\text{S}_{32}$  (T = Cr, Mo, W): Toward Functionalization of the Conductive “Cu–S” Network. *Adv. Energy Mater.* **2019**, *9*, 1803249.
- (26) Guérou, G.; Lemoine, P.; Raveau, B.; Guilmeau, E. Recent Developments in High-Performance Thermoelectric Sulphides: An Overview of the Promising Synthetic Colusites. *J. Mater. Chem. C* **2021**, *9*, 773–795.
- (27) Long, S. O. J.; Powell, A. V.; Vaqueiro, P.; Hull, S. High Thermoelectric Performance of Bornite through Control of the Cu(II) Content and Vacancy Concentration. *Chem. Mater.* **2018**, *30*, 456–464.
- (28) Freer, R.; Ekren, D.; Ghosh, T.; Biswas, K.; Qiu, P.; Wan, S.; Chen, L.; Han, S.; Fu, C.; Zhu, T.; Ashiqzaman Shawon, A. K. M.; Zevalkink, A.; Imasato, K.; Snyder, G. J.; Ozen, M.; Saglik, K.; Aydemir, U.; Cardoso-Gil, R.; Svanidze, E.; Funahashi, R.; Powell, A. V.; Mukherjee, S.; Tippireddy, S.; Vaqueiro, P.; Gascoin, F.; Kyratsi, T.; Sauerstich, P.; Mori, T. Key Properties of Inorganic Thermoelectric Materials—Tables (Version 1). *J. Phys. Energy* **2022**, *4*, 022002.
- (29) Biswas, K.; Zhao, L.-D.; Kanatzidis, M. G. Tellurium-Free Thermoelectric: The Anisotropic n-Type Semiconductor  $\text{Bi}_2\text{S}_3$ . *Adv. Energy Mater.* **2012**, *2*, 634–638.
- (30) Zhao, J.; Hao, S.; Islam, S. M.; Chen, H.; Tan, G.; Ma, S.; Wolverton, C.; Kanatzidis, M. G. Six Quaternary Chalcogenides of the Pavonite Homologous Series with Ultralow Lattice Thermal Conductivity. *Chem. Mater.* **2019**, *31*, 3430–3439.
- (31) Maji, K.; Lemoine, P.; Renaud, A.; Zhang, B.; Zhou, X.; Carnevali, V.; Candolfi, C.; Raveau, B.; Al Rahal Al Orabi, R.; Fornari, M.; Vaqueiro, P.; Pasturel, M.; Prestipino, C.; Guilmeau, E. A Tunable Structural Family with Ultralow Thermal Conductivity: Copper-Deficient  $\text{Cu}_{1-x}\text{Pb}_{1-x}\text{Bi}_x\text{S}_3$ . *J. Am. Chem. Soc.* **2022**, *144*, 1846–1860.
- (32) Liang, H.; Guo, J.; Zhou, Y.-X.; Wang, Z.-Y.; Feng, J.; Ge, Z.-H.  $\text{CuPbBi}_3\text{S}_9$  Thermoelectric Material with an Intrinsic Low Thermal Conductivity: Synthesis and Properties. *J. Materiomics* **2022**, *8*, 174–183.
- (33) Mumme, W. G.; Welin, E.; Wuensch, B. J. Crystal Chemistry and Proposed Nomenclature for Sulfosalts Intermediate in the System Bismuthinite-Aikinite ( $\text{Bi}_2\text{S}_3\text{-CuPbBiS}_3$ ). *Am. Mineral.* **1976**, *61*, 15–20.
- (34) Harris, D. C.; Chen, T. T. Crystal Chemistry and Re-Examination of Nomenclature of Sulfosalts in the Aikinite-Bismuthinite Series. *Can. Mineral.* **1976**, *14*, 194–205.
- (35) Chen, T. T.; Kirchner, E.; Paar, W. Friedrichite  $\text{Cu}_3\text{Pb}_3\text{Bi}_3\text{S}_{18}$ , a New Member of the Aikinite-Bismuthinite Series. *Can. Mineral.* **1978**, *16*, 127–130.
- (36) Pring, A. Annealing of Synthetic Hammarite,  $\text{Cu}_2\text{Pb}_2\text{Bi}_4\text{S}_9$ , and the Nature of Cation-Ordering Processes in the Bismuthinite-Aikinite Series. *Am. Mineral.* **1995**, *80*, 1166–1173.
- (37) Cahill, D. G.; Watson, S. K.; Pohl, R. O. Lower Limit to the Thermal Conductivity of Disordered Crystals. *Phys. Rev. B: Condens. Matter Phys.* **1992**, *46*, 6131–6140.
- (38) Toby, B. H. EXPGUI, a Graphical User Interface for GSAS. *J. Appl. Crystallogr.* **2001**, *34*, 210–213.
- (39) Huq, A.; Kirkham, M.; Peterson, P. F.; Hodges, J. P.; Whitfield, P. S.; Page, K.; Hügle, T.; Iverson, E. B.; Parizzi, A.; Rennich, G. POWGEN: Rebuild of a Third-Generation Powder Diffractometer at the Spallation Neutron Source. *J. Appl. Crystallogr.* **2019**, *52*, 1189–1201.
- (40) Toby, B. H.; Von Dreele, R. B. GSAS-II: The Genesis of a Modern Open-Source All Purpose Crystallography Software Package. *J. Appl. Crystallogr.* **2013**, *46*, 544–549.
- (41) Tauc, J.; Grigorovici, R.; Vancu, A. Optical Properties and Electronic Structure of Amorphous Germanium. *Phys. Status Solidi B* **1966**, *15*, 627–637.
- (42) Kim, H. S.; Gibbs, Z. M.; Tang, Y.; Wang, H.; Snyder, G. J. Characterization of Lorenz Number with Seebeck Coefficient Measurement. *APL Mater.* **2015**, *3*, 041506.
- (43) Vaqueiro, P.; Mukherjee, S.; Powell, A. V.; Voneshen, D. J. Ultralow thermal conductivity in aikinite,  $\text{CuPbBiS}_3$ . <https://doi.org/10.5286/ISIS.E.RB2210076> (accessed on 08 22, 2022).
- (44) Arnold, O.; Bilheux, J. C.; Borreguero, J. M.; Buts, A.; Campbell, S. I.; Chapon, L.; Doucet, M.; Draper, N.; Ferraz Leal, R.; Gigg, M. A.; Lynch, V. E.; Markvardsen, A.; Mikkelsen, D. J.; Mikkelsen, R. L.; Miller, R.; Palmen, K.; Parker, P.; Passos, G.; Perring, T. G.; Peterson, P. F.; Ren, S.; Reuter, M. A.; Savici, A. T.; Taylor, J. W.; Taylor, R. J.; Tolchenov, R.; Zhou, W.; Zikovsky, J. Mantid—Data Analysis and Visualization Package for Neutron Scattering and  $\mu$  SR Experiments. *Nucl. Instrum. Methods Phys. Res. Sect. Accel. Spectrometers Detect. Assoc. Equip.* **2014**, *764*, 156–166.
- (45) Akeroyd, F.; Ansell, S.; Antony, S.; Arnold, O.; Bekasovs, A.; Bilheux, J.; Borreguero, J.; Brown, K.; Buts, A.; Campbell, S.; Champion, D.; Chapon, L.; Clarke, M.; Cottrell, S.; Dalglish, R.; Dillow, D.; Doucet, M.; Draper, N.; Fowler, R.; Gigg, M. A.; Granroth, G.; Hagen, M.; Heller, W.; Hillier, A.; Howells, S.; Jackson, S.; Kachere, D.; Koennecke, M.; Le Bourlot, C.; Leal, R.; Lynch, V.; Manuel, P.; Markvardsen, A.; McGreevy, R.; Mikkelsen, D.; Mikkelsen, R.; Miller, R.; Nagella, S.; Nielsen, T.; Palmen, K.; Parker, P. G.; Pascal, M.; Passos, G.; Perring, T.; Peterson, P. F.; Pratt, F.; Proffen, T.; Radaelli, P.; Rainey, J.; Ren, S.; Reuter, M.; Sastry, L.; Savici, A.; Taylor, J.; Taylor, R. J.; Thomas, M.; Tolchenov, R.; Whitley, R.; Whitty, M.; Williams, S.; Zhou, W.; Zikovsky, J. *Mantid: Manipulation and Analysis Toolkit for Instrument Data*, 2013.
- (46) Azuah, R. T.; Kneller, L. R.; Qiu, Y.; Tregenna-Piggott, P. L. W.; Brown, C. M.; Copley, J. R. D.; Dimeo, R. M. DAVE: A Comprehensive Software Suite for the Reduction, Visualization, and Analysis of Low Energy Neutron Spectroscopic Data. *J. Res. Natl. Inst. Stan. Technol* **2009**, *114*, 341.
- (47) Giannozzi, P.; Baroni, S.; Bonini, N.; Calandra, M.; Car, R.; Cavazzoni, C.; Ceresoli, D.; Chiarotti, G. L.; Cococcioni, M.; Dabo, I.; Dal Corso, A.; de Gironcoli, S.; Fabris, S.; Fratesi, G.; Gebauer, R.

- Gerstmann, U.; Gougoussis, C.; Kokalj, A.; Lazzeri, M.; Martin-Samos, L.; Marzari, N.; Mauri, F.; Mazzeo, R.; Paolini, S.; Pasquarello, A.; Paulatto, L.; Sbraccia, C.; Scandolo, S.; Scaluzero, G.; Seitsonen, A. P.; Smogunov, A.; Umari, P.; Wentzcovitch, R. M. QUANTUM ESPRESSO: A Modular and Open-Source Software Project for Quantum Simulations of Materials. *J. Phys. Condens. Matter* **2009**, *21*, 395502.
- (48) Supka, A. R.; Lyons, T. E.; Liyanage, L.; D'Amico, P.; Al Rahal Al Orabi, R.; Mahatara, S.; Gopal, P.; Toher, C.; Ceresoli, D.; Calzolari, A.; Curtarolo, S.; Nardelli, M. B.; Fornari, M. AFLOWx: A minimalist approach to high-throughput ab initio calculations including the generation of tight-binding hamiltonians. *Comput. Mater. Sci.* **2017**, *136*, 76–84.
- (49) Agapito, L. A.; Curtarolo, S.; Buongiorno Nardelli, M. Reformulation of DFT + U as a Pseudohybrid Hubbard Density Functional for Accelerated Materials Discovery. *Phys. Rev. X* **2015**, *5*, 011006.
- (50) Monkhorst, H. J.; Pack, J. D. Special Points for Brillouin-Zone Integrations. *Phys. Rev. B: Solid State* **1976**, *13*, 5188–5192.
- (51) Supka, A.; Mecholsky, N. A.; Buongiorno Nardelli, M.; Curtarolo, S.; Fornari, M. Two-Layer High-Throughput: Effective Mass Calculations Including Warping. *Engineering* **2022**, *10*, 74–80.
- (52) Kühne, T. D.; Iannuzzi, M.; Del Ben, M.; Rybkin, V. V.; Seewald, P.; Stein, F.; Laino, T.; Khaliullin, R. Z.; Schütt, O.; Schiffmann, F.; Golze, D.; Wilhelm, J.; Chulkov, S.; Bani-Hashemian, M. H.; Weber, V.; Borstnik, U.; Taillefumier, M.; Jakobovits, A. S.; Lazzaro, A.; Pabst, H.; Müller, T.; Schade, R.; Guidon, M.; Andermatt, S.; Holmberg, N.; Schenter, G. K.; Hehn, A.; Bussy, A.; Belleflamme, F.; Tabacchi, G.; Glöß, A.; Lass, M.; Bethune, L.; Mundy, C. J.; Plessl, C.; Watkins, M.; VandeVondele, J.; Krack, M.; Hutter, J. CP2K: An Electronic Structure and Molecular Dynamics Software Package - Quickstep: Efficient and Accurate Electronic Structure Calculations. *J. Chem. Phys.* **2020**, *152*, 194103.
- (53) VandeVondele, J.; Hutter, J. Gaussian Basis Sets for Accurate Calculations on Molecular Systems in Gas and Condensed Phases. *J. Chem. Phys.* **2007**, *127*, 114105.
- (54) Bussi, G.; Donadio, D.; Parrinello, M. Canonical Sampling through Velocity Rescaling. *J. Chem. Phys.* **2007**, *126*, 014101.
- (55) Marzari, N.; Mostofi, A. A.; Yates, J. R.; Souza, I.; Vanderbilt, D. Maximally Localized Wannier Functions: Theory and Applications. *Rev. Mod. Phys.* **2012**, *84*, 1419–1475.
- (56) Berghold, G.; Mundy, C. J.; Romero, A. H.; Hutter, J.; Parrinello, M. General and Efficient Algorithms for Obtaining Maximally Localized Wannier Functions. *Phys. Rev. B: Condens. Matter Mater. Phys.* **2000**, *61*, 10040–10048.
- (57) Remsing, R. C.; Klein, M. L. Lone Pair Rotational Dynamics in Solids. *Phys. Rev. Lett.* **2020**, *124*, 066001.
- (58) Zhang, Y. First-Principles Debye–Callaway Approach to Lattice Thermal Conductivity. *J. Mater. Chem.* **2016**, *2*, 237–247.
- (59) Zhang, Y.; Skoug, E.; Cain, J.; Ozoliņš, V.; Morelli, D.; Wolverton, C. First-Principles Description of Anomalously Low Lattice Thermal Conductivity in Thermoelectric Cu-Sb-Se Ternary Semiconductors. *Phys. Rev. B: Condens. Matter Mater. Phys.* **2012**, *85*, 054306.
- (60) Kohatsu, I.; Wuensch, B. J. The Crystal Structure of Aikinite,  $\text{PbCuBiS}_3$ . *Acta Crystallogr. Sect. B* **1971**, *27*, 1245–1252.
- (61) Ohmasa, M.; Nowacki, W. A redetermination of the crystal structure of aikinite  $[\text{BiS}_2/\text{S}/\text{CuIVPbVII}]$ . *Z. Für Krist. - Cryst. Mater.* **1970**, *132*, 71–86.
- (62) Baur, W. H. The Geometry of Polyhedral Distortions. Predictive Relationships for the Phosphate Group. *Acta Crystallogr. Sect. B* **1974**, *30*, 1195–1215.
- (63) Lundegaard, L. F.; Makovicky, E.; Boffa-Ballaran, T.; Balic-Zunic, T. Crystal Structure and Cation Lone Electron Pair Activity of  $\text{Bi}_2\text{S}_3$  between 0 and 10 GPa. *Phys. Chem. Miner.* **2005**, *32*, 578–584.
- (64) Cordero, B.; Gómez, V.; Platero-Prats, A. E.; Revés, M.; Echeverría, J.; Cremades, E.; Barragán, F.; Alvarez, S. Covalent Radii Revisited. *Dalton Trans.* **2008**, *21*, 2832–2838.
- (65) Shannon, R. D. Revised Effective Ionic Radii and Systematic Studies of Interatomic Distances in Halides and Chalcogenides. *Acta Crystallogr. Sect. A* **1976**, *32*, 751–767.
- (66) Batsanov, S. S. Van Der Waals Radii of Elements. *Inorg. Mater.* **2001**, *37*, 871–885.
- (67) Koumpouras, K.; Larsson, J. A. Distinguishing between Chemical Bonding and Physical Binding Using Electron Localization Function (ELF). *J. Phys. Condens. Matter* **2020**, *32*, 315502.
- (68) Remsing, R. C.; Klein, M. L. A New Perspective on Lone Pair Dynamics in Halide Perovskites. *APL Mater.* **2020**, *8*, 050902.
- (69) Dutta, M.; Samanta, M.; Ghosh, T.; Voneshen, D. J.; Biswas, K. Evidence of Highly Anharmonic Soft Lattice Vibrations in a Zintl Rattler. *Angew. Chem.* **2021**, *133*, 4305–4311.
- (70) Luu, S. D. N.; Supka, A. R.; Nguyen, V. H.; Vo, D.-V. N.; Hung, T. N.; Wojciechowski, K. T.; Fornari, M.; Vaqueiro, P.; Vaqueiro, P. Origin of Low Thermal Conductivity in  $\text{In}_4\text{Se}_3$ . *ACS Appl. Energy Mater.* **2020**, *3*, 12549–12556.
- (71) Jana, M. K.; Pal, K.; Warankar, A.; Mandal, P.; Waghmare, U. V.; Biswas, K. Intrinsic Rattler-Induced Low Thermal Conductivity in Zintl Type  $\text{TlInTe}_2$ . *J. Am. Chem. Soc.* **2017**, *139*, 4350–4353.
- (72) Bhui, A.; Dutta, M.; Mukherjee, M.; Rana, K. S.; Singh, A. K.; Soni, A.; Biswas, K. Ultralow Thermal Conductivity in Earth-Abundant  $\text{Cu}_{1.6}\text{Bi}_{4.8}\text{S}_8$ : Anharmonic Rattling of Interstitial Cu. *Chem. Mater.* **2021**, *33*, 2993–3001.
- (73) Laurita, G.; Seshadri, R. Chemistry, Structure, and Function of Lone Pairs in Extended Solids. *Acc. Chem. Res.* **2022**, *55*, 1004–1014.
- (74) Chmielowski, R.; Péré, D.; Bera, C.; Opahle, I.; Xie, W.; Jacob, S.; Capet, F.; Roussel, P.; Weidenkaff, A.; Madsen, G. K. H.; Dennler, G. Theoretical and Experimental Investigations of the Thermoelectric Properties of  $\text{Bi}_2\text{S}_3$ . *J. Appl. Phys.* **2015**, *117*, 125103.
- (75) Hanus, R.; Agne, M. T.; Rettie, A. J. E.; Chen, Z.; Tan, G.; Chung, D. Y.; Kanatzidis, M. G.; Pei, Y.; Voorhees, P. W.; Snyder, G. J. Lattice Softening Significantly Reduces Thermal Conductivity and Leads to High Thermoelectric Efficiency. *Adv. Mater.* **2019**, *31*, 1900108.
- (76) Agne, M. T.; Hanus, R.; Snyder, G. J. Minimum Thermal Conductivity in the Context of Diffuson-Mediated Thermal Transport. *Energy Environ. Sci.* **2018**, *11*, 609–616.
- (77) Lin, S.; Li, W.; Li, S.; Zhang, X.; Chen, Z.; Xu, Y.; Chen, Y.; Pei, Y. High Thermoelectric Performance of  $\text{Ag}_9\text{GaSe}_6$  Enabled by Low Cutoff Frequency of Acoustic Phonons. *Joule* **2017**, *1*, 816–830.
- (78) Balijapelly, S.; Hauble, A.; Sundaramoorthy, S.; Watts, J. L.; Kaulzarich, S. M.; Chernatynskiy, A.; Choudhury, A. Ultralow Lattice Thermal Conductivity in the Aikinite Structure Family,  $\text{Cu}_x\text{Pb}_x\text{Bi}_{2-x}\text{S}_3$ , and Thermoelectric Properties of  $\text{Cu}_{0.14}\text{Pb}_{0.14}\text{Bi}_{1.86}\text{S}_3$ . *ACS Appl. Energy Mater.* **2022**, *5*, 14222–14230.
- (79) Shiga, T.; Shiomi, J.; Ma, J.; Delaire, O.; Radzynski, T.; Lusakowski, A.; Esfarjani, K.; Chen, G. Microscopic Mechanism of Low Thermal Conductivity in Lead Telluride. *Phys. Rev. B: Condens. Matter Mater. Phys.* **2012**, *85*, 155203.
- (80) Voneshen, D. J.; Refson, K.; Borissenko, E.; Krisch, M.; Bosak, A.; Piovano, A.; Cemal, E.; Enderle, M.; Gutmann, M. J.; Hoesch, M.; Roger, M.; Gannon, L.; Boothroyd, A. T.; Uthayakumar, S.; Porter, D. G.; Goff, J. P. Suppression of Thermal Conductivity by Rattling Modes in Thermoelectric Sodium Cobaltate. *Nat. Mater.* **2013**, *12*, 1028–1032.
- (81) Nilsson, G.; Nelin, G. Phonon Dispersion Relations in Ge at 80 K. *Phys. Rev. B: Solid State* **1971**, *3*, 364–369.
- (82) Xie, H.; Hao, S.; Bao, J.; Slade, T. J.; Snyder, G. J.; Wolverton, C.; Kanatzidis, M. G. All-Inorganic Halide Perovskites as Potential Thermoelectric Materials: Dynamic Cation off-Centering Induces Ultralow Thermal Conductivity. *J. Am. Chem. Soc.* **2020**, *142*, 9553–9563.